

Satellite Quantum Communications: Fundamental Bounds and Practical Security

Stefano Pirandola

Department of Computer Science, University of York, York YO10 5GH, United Kingdom

Satellite quantum communications are emerging within the panorama of quantum technologies as a more effective strategy to distribute completely-secure keys at very long distances, therefore playing an important role in the architecture of a large-scale quantum network. In this work, we apply and extend recent results in free-space quantum communications to determine the ultimate limits at which secret (and entanglement) bits can be distributed via satellites. Our study is comprehensive of the various practical scenarios, encompassing both downlink and uplink configurations, with satellites at different altitudes and zenith angles. It includes effects of diffraction, extinction, background noise and fading, due to pointing errors and atmospheric turbulence. Besides identifying upper bounds, we also discuss lower bounds, i.e., achievable rates for key generation and entanglement distribution. In particular, we study the composable finite-size secret key rates that are achievable by protocols of continuous variable quantum key distribution, for both downlink and uplink. Finally, we present a feasibility study with a sun-synchronous satellite whose performance in terms of key rate is compared with that of a chain of ideal quantum repeaters on the ground.

I. INTRODUCTION

Satellite quantum communications [1, Sec. VI] represent a new collective endeavour of the scientific community, with pioneering experiments already demonstrated. A number of quantum protocols have been successfully realized, including satellite-to-ground quantum key distribution (QKD) [2–4], entanglement distribution [5], entanglement-based QKD [6, 7], and ground-to-satellite quantum teleportation [8]. Further experiments have considered a space lab (Tiangong-2 [9]), and microsatellites, such as SOCRATES [10] and CubeSats [11].

An important driving reason behind the development of free-space quantum communications with satellites is the possibility to by-pass fundamental limitations that restrict rates and distances achievable by ground-based fiber communications. It is in fact well known that the amount of secret bits or entanglement bits (ebits) that can be distributed through a lossy communication channel with transmissivity η cannot exceed its secret key capacity $-\log_2(1 - \eta)$ bits/use, also known as the repeaterless PLOB bound [12]. In a ground-based fiber link, the transmissivity decays exponentially with the distance and so does the communication rate of any protocol for QKD or entanglement distribution.

One strategy to mitigate such a problem is the introduction of quantum repeaters or relays [1, Sec. XII]. In QKD the cheapest solution is the use of a chain of trusted nodes between the two end-users. These nodes distribute pairs of keys with their neighbours, whose composition via one-time pad generates a final secret key for the remote users. Here a non-trivial issue is the fact that all the nodes need to be trusted, so that the longer is the chain, the higher is the probability that security could be compromised. An alternative strategy relies in the adoption of nodes able to distribute entanglement, which is then swapped to the remote users. However, this solution is rather expensive because it involves the development of

quantum repeaters with long coherence times and distillation capabilities.

In this scenario, satellites open the way for new opportunities. Free-space connection with a satellite may have far less decibels of loss than a long ground-based fiber connection. Furthermore, most satellites are fast-moving objects, therefore able to physically travel between two far locations over the globe. These features have the potential to drastically reduce the complexity of a ground-based quantum network. In fact, a chain of nodes could just be replaced by a single satellite acting as a trusted QKD node or as a distributor of entanglement. In such an exciting new setting, it is crucial to understand the optimal performances allowed by quantum mechanics, and also what practical performances may be achieved with current technology. This work serves for this purpose.

Here we establish the information-theoretic limits of satellite quantum communications and also show their practical security on the basis of state-of-the-art technology. Our study extends the free-space analysis of Ref. [13], there developed for ground-to-ground free-space communications, to the more general setting of ground-satellite communications, where the optical signals travel slant distances with variable altitudes and zenith angles (in uplink or downlink). This scenario involves more general models for the underlying physical processes occurring within the atmosphere (refraction, extinction and turbulence), and different descriptions for the background noise (planetary albedos besides sky brightness). Accounting for these accurate models, we study the ultimate rates for secret key generation and entanglement distribution with a satellite in all scenarios (uplink/downlink, night/day-time operations).

Once we established the ultimate converse rates for secret key and entanglement distribution, we also study lower bounds. In particular, we focus our investigation on the practical rates that are achievable by a coherent-state QKD protocol, suitably modified to account for the fading channel between satellite and ground station, and

including the orbital dynamics of the satellite. Our security analysis considers finite-size effects and composable aspects. We show that secure high-rate QKD with continuous variable (CV) systems [14] is feasible for both downlink and uplink.

Moreover, we show that the number of secret key bits per day that can be distributed between two stations by a sun-synchronous satellite can be much larger than what achievable by a standard fiber connection between these stations, even when a substantial number of repeaters are employed in the middle and assumed to operate at their capacity level [15]. This analysis proves the potential advantages of satellite links over ground networks and strongly corroborates their role for near-future realization of large-scale quantum communications.

II. MAIN RESULTS

A. Geometric considerations

Consider a ground station (G), at some relatively-low altitude $h_0 \simeq 0$ above the sea level, and a satellite (S), that is orbiting at some variable altitude h beyond the Kármán line ($h \geq 100$ km) with a variable zenith angle θ . The latter is the angle between the zenith point at the ground station and the direction of observation pointing at the satellite. It takes positive values between 0 (satellite at the zenith) and $\pi/2$ (satellite at the horizon). In the case of a zenith-crossing orbit, it may also be useful to associate a sign to θ , so that $+\pi/2$ represents the forward horizon and $-\pi/2$ is the backward horizon.

Calling $R_E \simeq 6371$ km the approximate radius of the Earth, the slant distance z between the ground station and the satellite can be written as

$$z(h, \theta) = \sqrt{h^2 + 2hR_E + R_E^2 \cos^2 \theta - R_E \cos \theta}. \quad (1)$$

Equivalently, the altitude h of the satellite reads

$$h(z, \theta) = \sqrt{R_E^2 + z^2 + 2zR_E \cos \theta - R_E}. \quad (2)$$

See Appendix A for more details on this geometry, which can be easily extended to the case of non-negligible atmospheric altitudes h_0 for the ground station. (We remark that, while this extension may be useful, in our main text we investigate the basic scenario of a low-altitude ground station for which h_0 can be considered to be negligible with respect to the typical satellite altitudes.)

The formulas above are very good approximations for angles $\theta \lesssim 1$ (i.e., within about 60° from the zenith). For larger zenith angles, one needs to consider the apparent angle and the optical-path elongation induced by atmospheric refraction, which become more and more prominent close to the horizon. In such a case, the formulas above undergo some modifications as discussed in Appendix B. In our main text below, we omit this technicality for two reasons: (i) formulas above can still be

used to provide (larger) upper-bounds in the proximity of the horizon; (ii) when we treat achievable rates (lower bounds), we will restrict our study to the good window $\theta \lesssim 1$, an assumption which is also justified by the analysis of turbulence carried out later on in the manuscript.

In terms of configurations, we consider both uplink and downlink. In uplink, the ground station is the transmitter (Alice) and the satellite is the receiver (Bob); in downlink, it is the satellite to be the transmitter and the ground station to operate as a receiver. In these two configurations, the effects of free-space diffraction and atmospheric extinction are the same. Different is the case for the fading induced by turbulence (more relevant in uplink) and the thermal noise induced by background sources (with further differences between day- and night-time operations). For the sake of simplicity, we start by accounting for diffraction and extinction only; then, we will introduce the other effects, which need to be treated quite differently with respect to the models that are valid for ground-to-ground free-space communications.

B. Free-space diffraction

We assume that free-space quantum communication is based on a quasi-monochromatic optical mode with temporal duration Δt and narrow bandwidth $\Delta\lambda$ around a carrier wavelength λ (so that the angular frequency is $\omega = 2\pi c/\lambda$ and the wavenumber is $k = \omega/c = 2\pi/\lambda$). This model is represented by a Gaussian beam with field spot size w_0 and curvature R_0 [16–19]. Spot size is sufficiently smaller than the transmitter’s aperture so that the latter does not induce relevant diffraction. After free-space propagation for a distance z , the beam is detected by a receiver whose telescope has a circular aperture with radius a_R . To fix the ideas, one can assume that the propagation direction is uplink so that the ground station is the transmitter, but the model is completely symmetric and applies to downlink in exactly the same way.

Because of the inevitable free-space diffraction, the waist of the beam will broaden during propagation. After travelling for a distance z , the beam is intercepted by the receiver that will see an increased spot size

$$w_d(z) = w_0 \sqrt{(1 - z/R_0)^2 + (z/z_R)^2}, \quad (3)$$

where $z_R := \pi w_0^2 \lambda^{-1}$ is the Rayleigh range. Due to the finite aperture a_R of the receiving telescope, only a fraction of the initial beam will be detected, and this fraction is given by the diffraction-induced transmissivity

$$\eta_d(z) = 1 - e^{-2a_R^2/w_d^2}. \quad (4)$$

In the far field $z_R \gg 1$, this can be approximated as

$$\eta_d \simeq \eta_d^{\text{far}} := \frac{2a_R^2}{w_d^2} \ll 1. \quad (5)$$

Using η_d with the PLOB bound [12], one finds that the maximum number of secret bits that can be distributed by the most general (adaptive) QKD protocols over the free-space communication channel is upper-bounded by [13]

$$\mathcal{U}(z) = \frac{2}{\ln 2} \frac{a_R^2}{w_d^2} \text{ bits per use.} \quad (6)$$

In other words, the secret key capacity K of the free-space channel must satisfy $K \leq \mathcal{U}$ and, similarly, this bound also holds for the channel's entanglement distribution capacity $E \leq K$ (which is the number of ebits per use of the channel that can be distributed by the most general adaptive protocols of entanglement distribution; see Ref. [12] for exact mathematical definitions).

Note that a focused beam ($R_0 = z$) optimizes the bound in Eq. (6) but, at long distances, optical focusing becomes a very challenging task. For this reason, a better strategy is to just generate a collimated beam ($R_0 = \infty$) so that Eq. (6) is computed by assuming

$$w_d(z) = w_0 \sqrt{1 + z^2/z_R^2}. \quad (7)$$

We will therefore use the specific case of a collimated Gaussian beam in our numerical investigations.

It is also clear that $\mathcal{U}(z)$ can be expressed in terms of the altitude h and zenith angle θ of the satellite. In fact, we may replace the function $z = z(h, \theta)$ of Eq. (1) in Eq. (6) to get the expression for $\mathcal{U}(h, \theta) = \mathcal{U}[z(h, \theta)]$. The diffraction-bound $\mathcal{U}(h, \theta)$ is numerically investigated in Fig. 1, for a collimated Gaussian beam and a typical choice of parameters. In particular, we show this ultimate bound in two extreme angles for the satellite, i.e., zenith position ($\theta = 0$) and horizon ($\theta = \pi/2$). The reduction of the rate at the horizon is due to the greater slant distance to be travelled by the beam. As mentioned before, in this case the bound is optimistic because the refraction-induced elongation of the optical path is here neglected.

C. Atmospheric extinction

Another important physical process that causes loss in the free-space propagation of an optical beam is atmospheric extinction; this is induced by both aerosol absorption and Rayleigh/Mie scattering. For a free-space communication at fixed altitude h , this effect is described by the simple Beer-Lambert equation

$$\eta_{\text{atm}}(h) = \exp[-\alpha(h)z], \quad (8)$$

where $\alpha(h)$ is the extinction factor [20, Ch. 11]. This is given by $\alpha(h) = \alpha_0 \exp(-h/\tilde{h})$, where h is expressed in meters, $\tilde{h} = 6600$ m, and the sea-level value α_0 takes the value $\simeq 5 \times 10^{-6} \text{ m}^{-1}$ at $\lambda = 800 \text{ nm}$ [21, Sec. III.C].

It is clear that the model in Eq. (8) needs to be suitably modified in order to describe free-space optical communications at variable altitudes h . First suppose that the

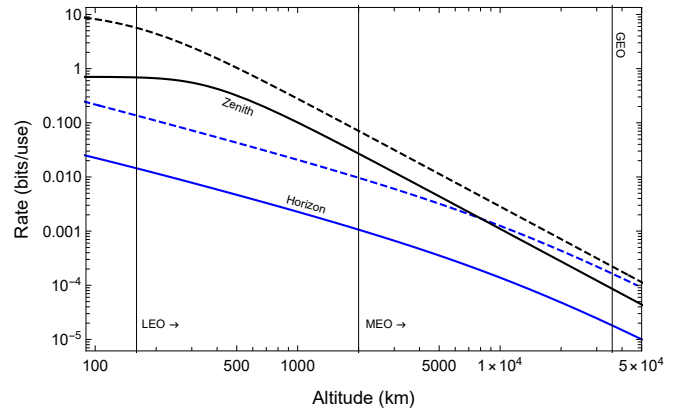


FIG. 1: Key rate between a ground station and a satellite at various altitudes h . In dashed we show the diffraction-based bound $\mathcal{U}(h, \theta)$ of Eq. (6) while, in solid, we show the upper-bound $\mathcal{V}(h, \theta)$ of Eq. (15) which includes the combined effects of diffraction, extinction and quantum efficiency. The upper black curves refer to the satellite at the zenith position ($\theta = 0$), while the lower blue curves refer to the horizon position ($\theta = \pi/2$). We assume a collimated Gaussian beam with $\lambda = 800 \text{ nm}$ and $w_0 = 20 \text{ cm}$, so that $z_R \simeq 160 \text{ km}$ (LEO boundary). Then, we assume $a_R = 40 \text{ cm}$ and $\eta_{\text{eff}} = 0.4$.

satellite is exactly at the zenith, so that its slant range z is equal to its altitude h . Then, we can easily compute

$$\begin{aligned} \eta_{\text{atm}}^{\text{zen}}(h) &= \exp \left[- \int_0^h dh' \alpha(h') \right] \\ &= \exp \left[\alpha_0 \tilde{h} (e^{-h/\tilde{h}} - 1) \right] \\ &\geq e^{-\alpha_0 \tilde{h}} \simeq 0.967 \quad (\simeq 0.14 \text{ dB}). \end{aligned} \quad (9)$$

The value in Eq. (9) is valid for any altitude and is already approximated at $h = 30 \text{ km}$, in the middle of the stratosphere, after which the atmospheric density is negligible. For this reason, for any satellite at the zenith position, we can use the estimate $\eta_{\text{atm}}^{\text{zen}}(\infty) \simeq 0.967$.

Consider now a generic zenith angle θ . Neglecting refraction, we can therefore use the expressions in Eqs. (1) and (2) and write the following expression for the atmospheric transmissivity

$$\eta_{\text{atm}}(h, \theta) = \exp \left\{ - \int_0^{z(h, \theta)} dy \alpha[h(y, \theta)] \right\} = e^{-\alpha_0 g(h, \theta)}, \quad (10)$$

where we have introduced the integral function

$$g(h, \theta) := \int_0^{z(h, \theta)} dy \exp \left[-\frac{h(y, \theta)}{\tilde{h}} \right]. \quad (11)$$

For zenith angles $\theta \lesssim 1$, one may check that Eq. (10) can be approximated as follows

$$\eta_{\text{atm}}(h, \theta) \simeq [\eta_{\text{atm}}^{\text{zen}}(h)]^{\sec \theta} \simeq [\eta_{\text{atm}}^{\text{zen}}(\infty)]^{\sec \theta}. \quad (12)$$

This approximation is already good at 30 km of altitude and becomes an almost exact formula beyond 100 km.

Combining atmospheric extinction with free-space diffraction and the inevitable internal loss η_{eff} affecting the setup of the receiver (due to non-unit quantum efficiency of the detector and other optical imperfections), we can write the total amount of fixed loss of the free-space channel from the generation of the Gaussian beam to its final detection. This is given by

$$\eta_{\text{tot}}(h, \theta) := \eta_{\text{eff}}\eta_{\text{atm}}(h, \theta)\eta_{\text{d}}(h, \theta), \quad (13)$$

where $\eta_{\text{d}}(h, \theta) = \eta_{\text{d}}[z(h, \theta)]$ and we can assume $\eta_{\text{eff}} \simeq 0.4$, i.e., about 4 dB (e.g., as in Ref. [22]). Using this transmissivity in the PLOB bound, we get an immediate extension of Ref. [13, Eq. (C5)], i.e.,

$$K \leq \mathcal{V}(h, \theta) := -\log_2[1 - \eta_{\text{tot}}(h, \theta)] \quad (14)$$

$$= -\log_2 \left[1 - \eta_{\text{eff}}e^{-\alpha_0 g(h, \theta)} \left(1 - e^{-\frac{2a_R^2}{w_{\text{d}}[z(h, \theta)]^2}} \right) \right] \quad (15)$$

$$\simeq \frac{2}{\ln 2} \frac{a_R^2 \eta_{\text{eff}} e^{-\alpha_0 g(h, \theta)}}{w_{\text{d}}[z(h, \theta)]^2}, \quad (16)$$

where the last approximation is valid for $\eta_{\text{tot}}(h, \theta) \ll 1$ which is certainly true in the far field regime $z_R \gg 1$.

From Fig. 1, we see that the combined effects of diffraction, extinction and non-ideal quantum efficiency decrease (by about one order of magnitude) the ultimate communication bounds that are only based on free-space diffraction. As for $\mathcal{U}(h, \theta)$, also the value of the upper bound $\mathcal{V}(h, \theta)$ is over-estimated at the horizon due to the fact that refraction has been neglected (see Appendix B for an extension of the bound which includes refraction). The ultimate performances discuss so far will further decrease when we include fading (turbulence/pointing errors) and then background noise.

D. Fading process induced by beam wandering: Turbulence and pointing errors

The combined transmissivity η_{tot} in Eq. (13) is constant for a fixed geometry, h and θ , between ground station and satellite. At each time instant, it corresponds to the maximum transmissivity which can be reached by a beam that is perfectly aligned between transmitter and receiver. In a realistic scenario, such alignment is however not maintained and we need to consider a process of beam wandering; this inevitably induces a fading process for the communication channel whose instantaneous transmissivity will fluctuate [23–26].

Beam wandering is due to random errors in the pointing mechanism of the transmitter and also to the action of atmospheric turbulence on a section of the optical path. These two effects are independent and they sum up. In practice, they have a different weights depending on the configuration. In downlink, pointing error is quite relevant, since on-board optics is limited, while turbulence can be neglected, because it occurs in the final section of the optical path where the beam has been already spread

by diffraction. In uplink, pointing error can be reduced, because ground stations may adopt more extensive and sophisticated optics; by contrast, turbulence represents a major effect in this case due to the fact that it affects the beam right after its generation.

In order to treat beam wandering and the corresponding fading process, we assume the regime of weak turbulence, which is appropriate for relatively-small zenith angles $\theta \lesssim 1$. In this regime, we may separate effects occurring on fast and slow time-scales. Turbulent eddies smaller than the beam waist act with a fast dynamics; these tend to broaden the beam, so that the diffraction-limited spot size w_{d} is replaced by a larger “short-term” spot size $w_{\text{st}} = w_{\text{st}}(z, \theta)$, also known as “hot spot”. On the other hand, turbulent eddies that are larger than the beam waist act on a much slower time scale [27] (of the order of 10–100 ms [28]); these tend to deflect the beam, whose centroid will then wander according to a Gaussian distribution with variance $\sigma_{\text{TB}}^2 = \sigma_{\text{TB}}^2(z, \theta)$. This slow dynamics can be fully resolved and closely followed by a fast detector, e.g., with a realistic bandwidth of the order of 100 MHz. On top of this process, there are pointing errors whose dynamics is also slow and causes an additional Gaussian random walk with variance $\sigma_{\text{P}}^2 \simeq (10^{-6}z)^2$ for a typical 1 μrad error at the transmitter. Overall, the wandering of the beam centroid has variance $\sigma^2 = \sigma_{\text{TB}}^2 + \sigma_{\text{P}}^2$.

A crucial theoretical step in our treatment is the explicit derivation of w_{st} and σ_{TB}^2 according to turbulence models that are appropriate for satellite communications. As discussed in detail in Appendix C, we start from the Hufnagel-Valley (H-V) model [29, 30], which provides the atmospheric profile for the refraction-index structure constant $C_n^2(h)$ [31, Sec. 12.2.1]. This altitude-dependent constant measures the strength of the fluctuations in the refraction index caused by spatial variations of temperature and pressure. Assuming this model, we then compute the scintillation index and the Rytov variance. The latter allows us to verify that the angular window $\theta \lesssim 1$ is compatible with the regime of weak turbulence, which is why we choose this angular window for quantum communication in both uplink and downlink.

From the structure constant $C_n^2(h)$, the wave-number k of the beam, and the geometry (slant distance z and zenith angle θ) one can define the spherical-wave coherence length $\rho_0 = \rho_0(z, \theta)$ for uplink (up) and downlink (down). Using the expression for generic z -long propagation [27, 32] and accounting for the altitude function $h = h(z, \theta)$ in Eq. (2), this length takes the form

$$\rho_0^{\text{up/down}} = \left[1.46k^2 \int_0^z d\xi \left(1 - \frac{\xi}{z} \right)^{\frac{5}{3}} \gamma^{\text{up/down}}(\xi) \right]^{-\frac{3}{5}},$$

$$\gamma^{\text{up}}(\xi) = C_n^2[h(\xi, \theta)], \quad \gamma^{\text{down}}(\xi) = C_n^2[h(z - \xi, \theta)]. \quad (17)$$

An analysis of ρ_0^{down} confirms that, within the good angular window and not-too large receiver apertures, downlink communication can be considered to be free of turbulence, so that we can set $\sigma_{\text{TB}}^2 \simeq 0$ and $w_{\text{st}} \simeq w_{\text{d}}$. By

contrast, for uplink communication, the value of ρ_0^{up} becomes rather small (of the order of 1 cm at $\lambda = 800$ nm), meaning that turbulence is relevant in this scenario. In this case, we can resort to Refs. [27, 33] and write analytical formulas for the short-term spot size and the variance of the centroid wandering.

For satellite distances one can easily check Yura's condition for uplink $\phi := 0.33(\rho_0^{\text{up}}/w_0)^{1/3} \ll 1$, whose validity allows us to write [33]

$$w_{\text{st}}^2 \simeq w_{\text{d}}^2 + 2 \left(\frac{\lambda z}{\pi \rho_0^{\text{up}}} \right)^2 \Psi, \quad (18)$$

$$\sigma_{\text{TB}}^2 \simeq \left(\frac{\lambda z}{\pi \rho_0^{\text{up}}} \right)^2 (1 - \Psi), \quad (19)$$

where $\Psi := (1 - \phi)^2 \simeq 1 - 2\phi$. For satellites in the LEO region and beyond, we can adopt the asymptotic planar approximation

$$\rho_0^{\text{up}} \simeq \rho_p^{\text{up}} \simeq [1.46k^2(\sec \theta)I_{\infty}]^{-3/5}, \quad (20)$$

$$I_{\infty} := \int_0^{\infty} d\xi C_n^2(\xi), \quad (21)$$

where ρ_p^{up} bounds the value of ρ_0^{up} from below at any relevant altitude and any $\theta \lesssim 1$ (e.g., see the comparison in Fig. 14 of Appendix C). This leads to the simpler expressions

$$w_{\text{st}}^2 \simeq w_{\text{d}}^2 + z^2 \Delta(\theta), \quad (22)$$

$$\sigma_{\text{TB}}^2 \simeq \frac{7.71I_{\infty}}{w_0^{1/3}} z^2 \sec \theta, \quad (23)$$

where we have set

$$\Delta(\theta) := \frac{26.28(I_{\infty} \sec \theta)^{6/5}}{\lambda^{2/5}} - \frac{7.71I_{\infty} \sec \theta}{w_0^{1/3}}. \quad (24)$$

In these formulas, I_{∞} takes different values depending on the parameters chosen for the H-V model. In particular, we compute $I_{\infty} \simeq 2.2354 \times 10^{-12} \text{ m}^{1/3}$ for the standard H-V_{5/7} model [31, Sec. 12.2.1], which is good for describing night-time operation. During the day, turbulence on the ground is higher and we consider a typical day-time version of the H-V model, for which $I_{\infty} \simeq 3.2854 \times 10^{-12} \text{ m}^{1/3}$ (see Appendix C for more details). Numerical investigations at $\lambda = 800$ nm show that w_{st} exceeds w_{d} by one order of magnitude in uplink, with an almost constant gap in the far field (e.g., see Fig. 15 in Appendix C). Finally, note that we re-obtain the downlink diffraction-limited values by setting $I_{\infty} = 0$ in Eqs. (22) and (23).

E. Bounds for the satellite fading channels in uplink and downlink

Following the theory of the previous section, it follows that we can adopt a unified approach to treat fading in

uplink and downlink. In fact, we may consider the general parameters w_{st} and $\sigma^2 = \sigma_{\text{TB}}^2 + \sigma_{\text{P}}^2$, which can then be simplified for the specific case of downlink, for which we may set $w_{\text{st}} \simeq w_{\text{d}}$ and $\sigma^2 \simeq \sigma_{\text{P}}^2$.

In general, the broader short-term spot size w_{st} decreases the maximum value of the transmissivity. In fact, the diffraction-induced transmissivity η_{d} has to be replaced by the (lower) short-term transmissivity

$$\eta_{\text{st}}(z, \theta) = 1 - e^{-2a_R^2/w_{\text{st}}^2}, \quad (25)$$

with far-field approximation

$$\eta_{\text{st}} \simeq \eta_{\text{st}}^{\text{far}} := \frac{2a_R^2}{w_{\text{st}}^2}. \quad (26)$$

As a result the combined expression η_{tot} of Eq. (13) has to be replaced by the more general parameter

$$\eta(h, \theta) := \eta_{\text{eff}} \eta_{\text{atm}}(h, \theta) \eta_{\text{st}}(h, \theta), \quad (27)$$

where $\eta_{\text{st}}(h, \theta) := \eta_{\text{st}}[z(h, \theta), \theta]$ using Eq. (1).

At any fixed geometry h and θ , the loss parameter $\eta(h, \theta)$ describes the maximum transmissivity that is achievable in the communication through the generally-turbulent free-space channel, which corresponds to the case where the incoming beam is perfectly aligned with the receiver's aperture. Note that, more generally, one may assume the case of a constant deflection for the beam; here we omit this technicality for two reasons: we are interested in the optimal rate performance of the communication and such a deflection can anyway be compensated by using adaptive optics.

As a consequence of beam wandering, the actual instantaneous value of the transmissivity will be $\tau \leq \eta$ and this value will depend on how far the beam is deflected from the center of the receiver's aperture. The Gaussian random walk of the beam centroid [34] results in a Weibull distribution for the instantaneous deflection which, in turn, leads to a probability distribution $P_{\text{fad}}(\tau)$ for the instantaneous transmissivity. Let us introduce the two functions

$$f_0(x) := [1 - \exp(-2x) I_0(2x)]^{-1}, \quad (28)$$

$$f_1(x) := \exp(-2x) I_1(2x), \quad (29)$$

in terms of the modified Bessel function I_n of the first kind with order $n = 0, 1$. These are useful to introduce the geometry-dependent positive parameters [26]

$$\gamma(z, \theta) = \frac{4\eta_{\text{st}}^{\text{far}} f_0(\eta_{\text{st}}^{\text{far}}) f_1(\eta_{\text{st}}^{\text{far}})}{\ln [2\eta_{\text{st}} f_0(\eta_{\text{st}}^{\text{far}})]}, \quad (30)$$

$$r_0(z, \theta) = \frac{a_R}{\{\ln [2\eta_{\text{st}} f_0(\eta_{\text{st}}^{\text{far}})]\}^{1/\gamma}}. \quad (31)$$

Using these parameters, we may then write

$$P_{\sigma}(\tau) = \frac{r_0^2}{\gamma \sigma^2 \tau} \left(\ln \frac{\eta}{\tau} \right)^{\frac{2}{\gamma} - 1} \exp \left[-\frac{r_0^2}{2\sigma^2} \left(\ln \frac{\eta}{\tau} \right)^{\frac{2}{\gamma}} \right]. \quad (32)$$

The free-space fading channel \mathcal{E}_{fad} can therefore be described by an ensemble $\{P_\sigma(\tau), \mathcal{E}_\tau\}$ of pure-loss channels \mathcal{E}_τ whose transmissivity τ is chosen with probability $P_{\text{fad}}(\tau)$. From the PLOB bound and the convexity of the relative entropy of entanglement [12], one has that the secret-key capacity of the fading channel \mathcal{E}_{fad} is bounded by the average

$$K \leq - \int_0^\eta d\tau P_\sigma(\tau) \log_2(1 - \tau). \quad (33)$$

Repeating the steps of Ref. [13, Appendix E], we may therefore re-obtain Ref. [13, Eq. (10)], i.e.,

$$K \leq \mathcal{B}(\eta, \sigma) := -\Delta(\eta, \sigma) \log_2(1 - \eta), \quad (34)$$

where $\Delta(\eta, \sigma)$ is defined by the expression

$$\Delta(\eta, \sigma) := 1 + \frac{\eta}{\ln(1 - \eta)} \int_0^{+\infty} dx \frac{\exp\left(-\frac{r_0^2}{2\sigma^2} x^2/\gamma\right)}{e^x - \eta}. \quad (35)$$

Note that, while Eq. (34) has exactly the same analytical form of the free-space bound in Ref. [13, Eq. (10)], it is here implicitly extended from the setting of ground-based communications to that of satellite communications. In $\mathcal{B}(\eta, \sigma)$, the component $-\log_2(1 - \eta) \simeq \eta/\ln 2$ upper-bounds the key rate achievable with a perfectly-aligned link between ground station and receiver, while $\Delta(\eta, \sigma)$ is a correction factor accounting for beam wandering, induced by turbulence and/or pointing errors. In order to investigate this bound for satellite communications, we need to include the necessary geometry and distinguish between downlink and uplink.

By replacing $z = z(h, \theta)$ in the formulas of γ , r_0 and the total variance σ^2 , we can express all these parameters in terms of h and θ . We may then use these functionals together with $\eta = \eta(h, \theta)$ of Eq. (27) in Eq. (34), so as to obtain a geometry-dependent expression for the bound $\mathcal{B} = \mathcal{B}(h, \theta)$. In Fig. 2, we investigate the behaviour of $\mathcal{B}(h, \theta)$ in uplink and downlink for a satellite at various altitudes h and for zenith angles equal to zero or 1. Besides the effects of free-space diffraction, atmospheric extinction and limited quantum efficiency, the downlink bound $\mathcal{B}_{\text{down}}(h, \theta)$ includes the centroid wandering due to pointing error σ_p^2 , while the uplink bound $\mathcal{B}_{\text{up}}(h, \theta)$ also includes turbulence-induced beam spreading (w_{st}) and wandering (so that $\sigma^2 = \sigma_p^2 + \sigma_{\text{TB}}^2$).

By comparing the zenith-performances of $\mathcal{B}_{\text{down}}$ in Fig. 1 and \mathcal{V} in Fig. 2, we can see how the pointing error decreases the rate already from the beginning of the LEO region. Then, by comparing the downlink bound $\mathcal{B}_{\text{down}}$ with the uplink bound \mathcal{B}_{up} Fig. 2, we see how turbulence induces a further non-trivial decrease, which is about one-two orders of magnitude. Also note that \mathcal{B}_{up} is additionally decreased during day time (while $\mathcal{B}_{\text{down}}$ does not depend on the operation time).

Several important considerations are in order about Eq. (34). The first is that, as long as the free-space fading channel \mathcal{E}_{fad} can indeed be described by an ensemble of instantaneous pure-loss channels \mathcal{E}_τ , i.e., $\mathcal{E}_{\text{fad}} =$

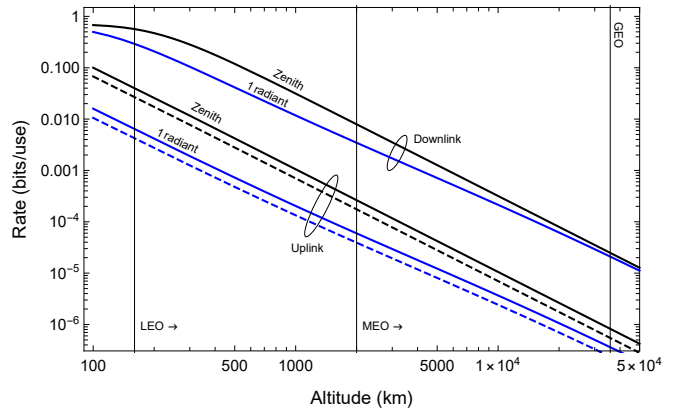


FIG. 2: Key rate between a ground station and a satellite at various altitudes h . We consider the upper-bound in Eq. (34) specified for downlink ($\mathcal{B}_{\text{down}}$) and uplink (\mathcal{B}_{up}), the latter being presented for night-time (solid) and day-time (dashed). In each case, we show the performance both at the zenith position ($\theta = 0$) and at $\theta = 1$ radian. In the various configurations, the lines upper-bound the maximum number of secret (and entanglement) bits that can be distributed per use of the channel, considering the combined effects of diffraction, atmospheric extinction, quantum efficiency, pointing error ($1 \mu\text{rad}$) and atmospheric turbulence (night-/day-time H-V model, only for uplink). As in Fig. 1, we assume a collimated beam with $\lambda = 800 \text{ nm}$ and $w_0 = 20 \text{ cm}$. Receiver has aperture $a_R = 40 \text{ cm}$ and total efficiency $\eta_{\text{eff}} = 0.4$.

$\{P_\sigma(\tau), \mathcal{E}_\tau\}$, then the bound \mathcal{B} in Eq. (34) is also achievable. As discussed in Ref. [13, Appendix F], this bound is achieved by optimal protocols of CV-QKD, either based on the use of quantum memories or employing largely-squeezed states in an extremely biased manner. The bound can also be achieved by optimal protocols of entanglement distribution, where distillation is assisted by one-way backward classical communication. The performance of these protocols is equal to the (bosonic) reverse coherent information [35], which achieves $-\log_2(1 - \tau)$ for each \mathcal{E}_τ . As a result, we may write $E = K = \mathcal{B}$ for both the entanglement distribution (E) and the secret key (K) capacities of the fading channel \mathcal{E}_{fad} .

The pure-loss assumption $\mathcal{E}_{\text{fad}} = \{P_\sigma(\tau), \mathcal{E}_\tau\}$, which implies the achievability of the bound \mathcal{B} , is appropriate for night-time operation at typical satellite altitudes. Different is the case for day-time operation, where the background noise becomes non-trivial. In this setting, the quantity \mathcal{B} in Eq. (34) is still an upper bound but no longer guaranteed to be achievable. In the following, we therefore consider a more refined upper bound and a corresponding lower bound in the presence of noise. These two bounds are useful for the study of day-time operation and also clarify the validity of the pure-loss assumption for night-time operation.

F. Satellite bounds with background noise

Let us account for the presence of background noise. First of all, it is important to adopt an appropriate model for the input-output number of photons. Call \bar{n}_T the mean number of photons that are present in the beam at the transmitter. For an instantaneous transmissivity τ , the mean number of photons reaching the receiver can be written as

$$\bar{n}_R = \tau \bar{n}_T + \bar{n}, \quad (36)$$

where \bar{n} is the mean number of thermal photons describing the overall noise affecting the propagation. Note that the thermal number \bar{n} does not depend on τ , so that the presence of noise does not lead to a passive signature. For this reason, the value of \bar{n} can be considered to be constant with respect to the fading process (in scenarios where this is not true, one maximizes this value over τ).

It is natural to decompose the thermal number \bar{n} as follows (see also Ref. [13, Fig. 1])

$$\bar{n} := \eta_{\text{eff}} \bar{n}_B + \bar{n}_{\text{ex}}, \quad (37)$$

where \bar{n}_B is the background thermal noise collected by the receiver's aperture, whose detector has quantum efficiency η_{eff} and extra noise \bar{n}_{ex} (in our numerical investigations of the upper bounds we set $\bar{n}_{\text{ex}} \simeq 0$). The value of \bar{n}_B depends on the operational setting (time of the day/direction of the link), besides features of the receiver, such as its aperture a_R , field of view Ω_{fov} , detection time Δt , carrier frequency λ and spectral filter $\Delta\lambda$.

Let us evaluate \bar{n}_B in the various settings. It is convenient to define the receiver's parameter

$$\Gamma_R := \Delta\lambda \Delta t \Omega_{\text{fov}} a_R^2. \quad (38)$$

Assuming $\Delta\lambda = 1 \text{ nm}$ and $\Delta t = 10 \text{ ns}$ for the detector, and $\Omega_{\text{fov}} = 10^{-10} \text{ sr}$ and $a_R = 40 \text{ cm}$ for the receiving telescope, we compute $\Gamma_R = 1.6 \times 10^{-19} \text{ m}^2 \text{ s nm sr}$.

Then, for uplink we may write

$$\bar{n}_B^{\text{up}} = \kappa H_{\lambda}^{\text{sun}} \Gamma_R, \quad (39)$$

where H_{λ}^{sun} is the solar spectral irradiance at the relevant wavelength λ , e.g., $H_{\lambda}^{\text{sun}} = 4.61 \times 10^{18} \text{ photons m}^{-2} \text{ s}^{-1} \text{ nm}^{-1} \text{ sr}^{-1}$ at $\lambda = 800 \text{ nm}$. In the formula above, the dimensionless parameter κ depends on the geometry and albedos of the Earth and the Moon. Its value is $\kappa_{\text{day}} \simeq 0.3$ for day-time and $\kappa_{\text{night}} \simeq 7.36 \times 10^{-7}$ for full-Moon night-time (see Appendix D for more details). For downlink, we instead have

$$\bar{n}_B^{\text{down}} = H_{\lambda}^{\text{sky}} \Gamma_R, \quad (40)$$

where H_{λ}^{sky} is the spectral irradiance of the sky in units of $\text{photons m}^{-2} \text{ s}^{-1} \text{ nm}^{-1} \text{ sr}^{-1}$. At $\lambda = 800 \text{ nm}$, its value ranges from 1.9×10^{13} (full-Moon clear night) to 1.9×10^{16} (clear day-time) and 1.9×10^{18} (cloudy day-time).

A summary of the resulting values for the mean number of photons is provided in Table I. These values confirm that background noise is practically negligible at night time, while it plays an important role for day time. Under general sky conditions, day-time operations need to be described by thermal-loss channels, where loss and fading effects are combined with the thermal bath collected by the field of view of the receiver.

	Day	Night
Downlink	$\simeq 0.3$ (cloudy) $\simeq 3 \times 10^{-3}$ (clear)	$\simeq 3 \times 10^{-6}$
Uplink	$\simeq 0.22$	$\simeq 5.4 \times 10^{-7}$

TABLE I: Environmental noise in satellite communications (mean number of thermal photons \bar{n}_B per mode). This is shown for uplink and downlink in various conditions, considering a typical receiver ($\Gamma_R = 1.6 \times 10^{-19} \text{ m}^2 \text{ s nm sr}$).

It is important to observe that the total input-output relation of Eq. (36) from transmitter to receiver is equivalent to the action of a thermal-loss channel $\mathcal{E}_{\tau, \bar{n}}$ with transmissivity τ and environmental noise

$$\bar{n}_e = \bar{n} / (1 - \tau). \quad (41)$$

From the point of view of the generic quadrature \hat{x} of the mode (i.e., position \hat{q} or momentum \hat{p}), Eq. (36) corresponds to the following transformation

$$\hat{x}_T \rightarrow \hat{x}_R = \sqrt{\tau} \hat{x}_T + \xi_{\text{add}}, \quad (42)$$

where the additive noise variable ξ_{add} can be written as $\xi_{\text{add}} = \sqrt{1 - \tau} \hat{e}$, with \hat{e} being the quadrature of an environmental thermal mode. Therefore, the overall process can be represented as an effective beam-splitter of transmissivity τ mixing the input mode of the transmitter with an environmental thermal mode which has \bar{n}_e mean number of photons. At the output of the beam splitter, one mode is the one detected by the receiver, while the other mode goes back into the environment.

In the worst-case scenario, one assumes that Eve controls the input environmental mode, so that it is assumed to be part of a TMSV state in her hands (which realizes a purification of the channel, unique up to local isometries on the environment). One also assumes that all environmental modes after interaction are stored by Eve in a quantum memory to be subject to an optimal joint measurement. This active strategy is known as collective entangling-cloner attack and represents the most typical collective Gaussian attack [36]. According to Ref. [12], the relative entropy of entanglement suitably computed over the asymptotic Choi matrix of the thermal-loss channel $\mathcal{E}_{\tau, \bar{n}}$ provides an upper bound for its secret key capacity K . For each instantaneous channel $\mathcal{E}_{\tau, \bar{n}}$ describing the satellite link, we have $K(\mathcal{E}_{\tau, \bar{n}}) \leq \Phi_{\tau, \bar{n}}$,

where [12]

$$\Phi_{\tau, \bar{n}} = \begin{cases} -\log_2 [(1-\tau)\tau^{\bar{n}_e}] - h(\bar{n}_e), & \text{for } \bar{n} \leq \tau, \\ 0 & \text{for } \bar{n} > \tau, \end{cases} \quad (43)$$

and we have set $h(x) := (x+1)\log_2(x+1) - x\log_2 x$.

Because we may assume that \bar{n} does not depend on τ (or it is maximized over τ), the satellite fading channel in the presence of background noise can be represented by the ensemble $\mathcal{E}_{\text{fad}}^{\text{noi}} = \{P_\sigma(\tau), \mathcal{E}_{\tau, \bar{n}}\}$. By averaging $\Phi_{\tau, \bar{n}}$ over the fading process in τ , Ref. [13] computed the general free-space upper bound

$$K \leq \int_{\bar{n}}^{\eta} d\tau P_\sigma(\tau) \Phi_{\tau, \bar{n}} \leq \mathcal{B}(\eta, \sigma) - \mathcal{T}(\bar{n}, \eta, \sigma), \quad (44)$$

for $\bar{n} \leq \eta$ and where the thermal correction \mathcal{T} is given by

$$\begin{aligned} \mathcal{T}(\bar{n}, \eta, \sigma) &= \left\{ 1 - e^{-\frac{r_0^2}{2\sigma^2} [\ln(\eta/\bar{n})]^{2/\gamma}} \right\} \\ &\times \left[\frac{\bar{n} \log_2 \bar{n}}{1 - \bar{n}} + h(\bar{n}) \right] + \mathcal{B}(\bar{n}, \sigma). \end{aligned} \quad (45)$$

Similarly, one may write the lower bound [13]

$$K \geq E \geq \mathcal{B}(\eta, \sigma) - \int_0^{\eta} d\tau P_\sigma(\tau) h\left(\frac{\bar{n}}{1-\tau}\right) \quad (46)$$

$$\geq \mathcal{B}(\eta, \sigma) - h\left(\frac{\bar{n}}{1-\eta}\right), \quad (47)$$

which is based on the RCI and can be approximated by ideal implementations of CV-QKD protocols [13, 37].

The application of these formulas to the specific satellite models developed above allows us to bound the ultimate rates for key (and entanglement) distribution that are achievable in the presence of background noise. First of all, we see that the presence of thermal noise restricts the maximum slant distance for secure key generation to some finite value z_{max} . From Eq. (44), we see that the rate must be zero for $\bar{n} = \eta$ which leads to an upper bound for z_{max} . If we assume ideal conditions, where all the effects are negligible with the exception of diffraction and thermal noise, the over-optimistic threshold condition $\bar{n} = \eta_d$ would still restricts the range to some finite value. In fact, the latter leads to $\bar{n} \leq \sqrt{f_{0R}(z_{\text{max}})}$, where $f_{0R}(z) := \pi w_0 a_R / (\lambda z)$ is the Fresnel number product of the beam and the receiver. Then, using Eqs. (39) and (40), we get the following bounds for the maximum ranges in uplink and downlink

$$z_{\text{max}}^{\text{up}} \leq \frac{\Sigma}{\kappa H_\lambda^{\text{sun}}}, \quad z_{\text{max}}^{\text{down}} \leq \frac{\Sigma}{H_\lambda^{\text{sky}}}, \quad (48)$$

where we have set $\Sigma := \pi w_0 / (\lambda \Delta \lambda \Delta t \Omega_{\text{fov}} a_R)$.

As also noted in Ref. [13], it is interesting to discuss the effect of the receiver aperture a_R on the performance of the communication. While Eqs. (4) and (25) imply

that larger values of a_R are beneficial (because increasing the transmissivity of the link), Eqs. (38)-(40) instead imply that increasing a_R leads to higher values of background noise collected by the receiver, which is not beneficial. This second aspect is also clear from the bounds in Eq. (48) where, if we increase a_R (or any other parameter at the denominator of Σ), we then tend to reduce the maximum range. There is therefore a trade-off to account in the choice of a_R , that should take an intermediate value, given by the optimization of the bound in Eq. (44). When a_R is too large so that $\bar{n} \geq 1$, we certainly have entanglement breaking in Eq. (44) and no secure key generation is possible. In particular, it is sure that no key can be distributed in uplink for $\Gamma_R \geq (\kappa H_\lambda^{\text{sun}})^{-1}$ or in downlink for $\Gamma_R \geq 1/H_\lambda^{\text{sky}}$.

While Eq. (48) is particularly simple, tighter bounds on z_{max} can be obtained by directly imposing $\mathcal{B}(\eta, \sigma) = \mathcal{T}(\bar{n}, \eta, \sigma)$ and using Eqs. (39) and (40) for \bar{n} . For the typical regime of parameters considered in this study, the situation is the one depicted in Table II.

	Day	Night
Downlink	$\lesssim 650$ km (cloudy)	$\lesssim 2 \times 10^5$ km
	$\lesssim 6300$ km (clear)	
Uplink	$\lesssim 110$ km	$\lesssim 9 \times 10^4$ km

TABLE II: Maximum ranges for secure key distribution for uplink and downlink in various conditions, considering a typical receiver with $\Gamma_R = 1.6 \times 10^{-19} \text{ m}^2 \text{ s nm sr}$.

We observe that thermal noise represents quite an important limitation for day-time operation. As a matter of fact, day-time uplink does seem to be particularly challenging for satellite QKD. For the regime considered, the security range is roughly limited to the Kármán line. In order to reach LEO altitudes, we need better setup parameters. For instance, a faster detector working at 1 GHz (instead of 100 MHz) will reduce Γ_R and n_B^{up} by a factor of 10. As a result, we get a larger bound for the maximum range, i.e., $z_{\text{max}} \lesssim 340$ km. In downlink, day-time limitations appear to be less severe. For the considered regime, secret key generation is confined to the LEO region in a cloudy day, but may access MEO altitudes in a clear-sky day. In the following, we study the optimal scenario of clear-sky day-time downlink, together with the configurations of night-time downlink/uplink, whose security range exceeds GEO altitudes.

Following our preliminary analysis on the security ranges, we now explicitly study the thermal-loss upper bound in Eq. (44) for the cases of night-time downlink/uplink and day-time downlink (with clear sky). Numerical results are presented in Fig. 3.

For night-time downlink/uplink, one can numerically check that the thermal correction $\mathcal{T}(\bar{n}, \eta, \sigma)$ is practically negligible, so that the thermal-loss upper bound coincides with the loss-limited bound $\mathcal{B}(\eta, \sigma)$, with only

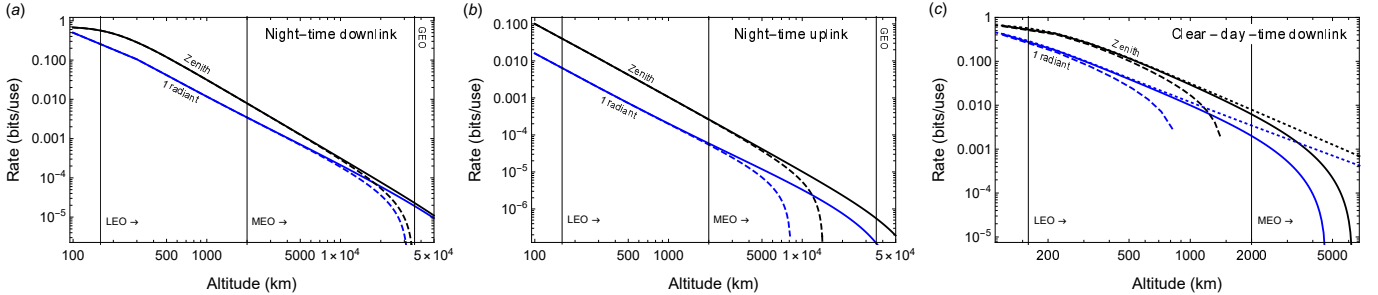


FIG. 3: Key rate between a ground station and a satellite at various altitudes h . In each configuration we consider the thermal-loss upper bound of Eq. (44) (solid lines) and the thermal-loss lower bound of Eq. (47) (dashed lines), specified for the satellite at the zenith position (black lines) or at 1 radian (blue lines). In particular, we consider night-time downlink in (a), night-time uplink in (b), and day-time downlink with clear sky in (c). For the latter case, we also show the performance of the loss-limited upper bound in Eq. (34) (dotted lines). As in previous figures, we consider diffraction, extinction, quantum efficiency, pointing error (1 μ rad) and atmospheric turbulence (H-V model). Collimated beam has $\lambda = 800$ nm and $w_0 = 20$ cm. Receiver has a telescope with $a_R = 40$ cm and $\Omega_{\text{fov}} = 10^{-10}$ sr, and a detector with $\Delta\lambda = 1$ nm, $\Delta t = 10$ ns, $\eta_{\text{eff}} = 0.4$ and $\bar{n}_{\text{ex}} = 0$. Therefore, the receiver has $\Gamma_R = 1.6 \times 10^{-19}$ m² s nm sr and the background thermal photons \bar{n}_B are those specified in Table I.

small deviations at GEO altitudes. Furthermore, as we can see from Figs. 3(a,b), the thermal-loss upper bound of Eq. (44) numerically coincides with the lower bound of Eq. (47) at LEO altitudes. This means that, for LEO satellites, the two bounds collapse into the loss-limited bound $\mathcal{B}(\eta, \sigma)$ which therefore represents the secret key capacity K (and entanglement-distribution capacity E) of the satellite channel. Said in other words, for night-time downlink/uplink and LEO altitudes, the free-space fading channel can certainly be approximated by an ensemble of pure-loss channels and we can write the achievability result $E \simeq K \simeq \mathcal{B}$. At higher altitudes in the MEO region, the presence of a gap does not allow us to enforce the pure-loss assumption and claim achievability (with respect to parameters chosen in our simulation).

For clear-day-time downlink in Fig. 3(c), the gap between the two thermal-loss bounds of Eqs. (44) and (47) already appears in the LEO region, even though at low altitudes (of the order of 160 km) there is a substantial coincidence. We can appreciate how, for increasing altitudes, not only the gap increases but the thermal-loss upper bound also substantially departs from the loss-limited bound $\mathcal{B}(\eta, \sigma)$, confirming the relevant role of the background thermal noise in limiting the rate performance for day-time operation.

It is important to remark that the achievability of the upper bound refers to a satellite *at a fixed* geometry, i.e., with fixed altitude and zenith angle. This means that we ignore the orbital dynamics or we assume that such a dynamics is much slower than the time-scale of the quantum communication, so that the channel is used many times before the satellite has substantially moved. However, apart from GEO satellites, the orbital dynamics is instead quite relevant and we therefore need to modify the form of the lower bound in order to account for this process.

Suppose that the rate in Eq. (44) can approximately be achieved after n pulses. Such a block of n pulses

corresponds to slice of the orbit over which we identify the larger (worst-case) values for h and θ . Then, an achievable rate would certainly be given by Eq. (44) computed over such values (but the upper bound would not be matched in all the slice). In the following, we consider the problem of orbital slicing more carefully for the derivation of a composable secret key rate

G. Composable finite-size security for satellite CV-QKD

Once we have clarified the ultimate limits for distributing keys (and entanglement) with satellites, we study the rates that are achievable by practical CV-QKD protocols, where we explicitly account for finite-size and composable aspects. We adopt the pilot-based protocol studied in Ref. [13], here suitably applied and extended to considering the underlying physical models valid for satellite communications. The idea is to use a coherent-state protocol, where Gaussian-modulated signal pulses (used to encode the information) are randomly interleaved with more energetic pilot pulses, that are used to monitor the instantaneous transmissivity of the satellite link in real-time (besides providing an estimate of the thermal noise). In this way, the parties are able to allocate the distributed data to slots of transmissivity and to perform classical post-processing slot-by-slot. Because the pilots are energetic, the allocation is practically flawless so that it does not introduce error-terms in the final rate.

In general, one may divide the interval $[0, \eta]$ by introducing a lattice with step $\delta\tau$, so that we have $M = \eta/\delta\tau$ slots $[\tau_k, \tau_{k+1}]$ with $\tau_k := k\delta\tau$ and $k = 0, \dots, M - 1$. When the k th slot is selected, with probability

$$p_k = \int_{\tau_k}^{\tau_{k+1}} d\tau P_\sigma(\tau), \quad (49)$$

the corresponding data points are associated to its mini-

imum transmissivity τ_k . A simpler post-selection strategy consists of introducing a threshold value η_{th} and only accepting data points with $\tau > \eta_{\text{th}}$, which happens with probability

$$p_{\text{th}} = \int_{\eta_{\text{th}}}^{\eta} d\tau P_{\sigma}(\tau). \quad (50)$$

Then, the data points allocated to the good slot are automatically associated to the threshold transmissivity η_{th} . Here we adopt this solution which is simpler and more robust, especially for long-distance communications.

1. Rate at fixed transmissivity

To fix the ideas, let us start by considering the link to be a thermal-loss channel $\mathcal{E}_{\tau, \bar{n}}$ with fixed transmissivity τ and thermal noise $\bar{n}_e = \bar{n}/(1 - \tau)$ with \bar{n} being specified by Eq. (37). In a coherent-state protocol [38, 39], the transmitter generates an input mode with generic quadrature $\hat{x}_T = x + \hat{v}$, where \hat{v} is the vacuum quadrature and x is a Gaussianly modulated variable with variance $\sigma_x^2 = \mu - 1$ (with μ being the variance of the average thermal state generated by the transmitter). At the output of the thermal-loss channel $\mathcal{E}_{\tau, \bar{n}}$, the receiver gets a mode with generic quadrature \hat{x}_R as given in Eq. (42). Assuming that the output is homodyned (randomly in \hat{q} or \hat{p}), then the receiver's classical outcome takes the form

$$y = \sqrt{\tau}x + z, \quad (51)$$

where z is a random noise variable, distributed according to a Gaussian with zero mean and variance $\sigma_z^2 = 2\bar{n} + 1$. If heterodyne is used, then the outcome y (for each of the two quadratures) is affected by thermal noise with larger variance $\sigma_z^2 + 1$.

For fixed τ and \bar{n} , one computes the mutual information $I(x : y | \tau, \bar{n})$ which takes simple expressions for the two types of output detections, i.e.,

$$I^{\text{hom}}(x : y | \tau, \bar{n}) = \frac{1}{2} \log_2 \left(1 + \frac{\tau \sigma_x^2}{2\bar{n} + 1} \right), \quad (52)$$

$$I^{\text{het}}(x : y | \tau, \bar{n}) = \log_2 \left(1 + \frac{\tau \sigma_x^2}{2\bar{n} + 2} \right). \quad (53)$$

Using the entanglement-based representation and reverse reconciliation, it is also easy to compute Eve's Holevo bound $\chi(E : y | \tau, \bar{n})$ with explicit expressions for χ^{hom} and χ^{het} that can be found in Ref. [13, Appendix H]. Therefore, one may write the asymptotic key rate against collective Gaussian attacks, which takes the form

$$R(\tau, \bar{n}) = \beta I(x : y | \tau, \bar{n}) - \chi(E : y | \tau, \bar{n}), \quad (54)$$

where $\beta \in [0, 1]$ is the reconciliation parameter (here βI corresponds to the effective rate of the code which is employed in the step of error correction).

As mentioned above, parameters τ and \bar{n} can be estimated using pilots, i.e., m energetic coherent-state pulses

$|\sqrt{n_p}e^{i\pi/4}\rangle$ interleaved with the quantum signals. The first moments of the pilots follow Eq. (51), where the magnitude of the noise z is negligible with respect to that of $\sqrt{\tau}x$. In particular, from the sampling variables $x_i = \sqrt{2\bar{n}_p}$ and $y_i = \sqrt{\tau}x_i + z_i$, we may build the estimator $\widehat{\sqrt{\tau}} := m^{-1} \sum_i y_i/x_i$ with mean $\sqrt{\tau}$ and variance $\sigma_z^2/(2m\bar{n}_p)$. The latter goes to zero for high \bar{n}_p even for very small m . The high energy regime is easily accessible using 10 ns-long pulses from a 100 mW laser source. At $\lambda = 800$ nm, each of these 1 nJ pulses contains an average of $x^2 \simeq 4 \times 10^9$ photons. In the worst case scenario of uplink communication to a GEO satellite at 1 radian, we have $\tau \simeq 4.4 \times 10^{-6}$ ($\simeq 53$ dB). The received energy would therefore be $\tau x^2 \simeq 1000 \gg \bar{n}$, where $\bar{n} < 1$.

The same classical pilots can be used for the estimation of the thermal noise \bar{n} [13]. From the instances x_i and y_i , we may build the estimator

$$\widehat{\bar{n}} = \frac{1}{2} \left[(mg)^{-1} \sum_i (y_i - \sqrt{\tau}x_i)^2 - g \right], \quad (55)$$

where $g = 1$ ($= 2$) for homodyne (heterodyne) detection. Parameter g accounts for the extra vacuum noise in the heterodyne detection and also for the fact that, for such a measurement, we have the double of data points, i.e., $2m$ pairs (x_i, y_i) for m pilots.

The estimator $\widehat{\bar{n}}$ is unbiased with variance $\sigma^2(\widehat{\bar{n}}) = (2\bar{n} + g)^2/(2gm) + \mathcal{O}(m^{-2})$ and can be used to construct the worst-case parameter

$$\bar{n}' := \widehat{\bar{n}} + w\sigma(\widehat{\bar{n}}) = \bar{n} + \frac{w}{\sqrt{2gm}}(2\bar{n} + g) + \mathcal{O}(m^{-1}), \quad (56)$$

which upper-bounds the actual thermal number \bar{n} up to an error probability ε_{pe} , with $w = \sqrt{2} \text{erf}^{-1}(1 - \varepsilon_{\text{pe}})$. Alternatively, one may write a more robust tail bound which leads to the same expression as in Eq. (56) but with $w = \sqrt{2 \ln(1/\varepsilon_{\text{pe}})}$. This can be used in the cases where ε_{pe} is very small, e.g., less than 10^{-17} [13].

It is therefore clear that the effect of parameter estimation is to modify the asymptotic rate in Eq. (54) as

$$R(\tau, \bar{n}) \rightarrow \frac{n}{N} R_m(\tau, \bar{n}'), \quad (57)$$

$$R_m(\tau, \bar{n}') = \beta I(x : y | \tau, \bar{n}') - \chi(E : y | \tau, \bar{n}'). \quad (58)$$

Parameter estimation provides the parties with crucial information about the amount of loss and noise present in the channel, so that they can apply a suitable code to correct their data. The procedure of error correction is successful with a probability p_{ec} which depends on the rate βI of the code and a pre-established ε -correctness ε_{cor} , which bounds the residual probability that the local strings are different after passing a hashing test. Thus, only np_{ec} pulses are successfully error-corrected and further processed into a key. This means that secret-key rate R_{pe} needs to be rescaled by the pre-factor

$$r_n := np_{\text{ec}}/N. \quad (59)$$

The next step is that of privacy amplification which is also not perfect. This means that there will be some non-zero distance between the final strings (composing the shared key) and an ideal classical-classical-quantum state where the eavesdropper is completely de-correlated from the parties. Such a distance is bounded by some target value of the ε -secrecy of the protocol, which is further decomposed as $\varepsilon_{\text{sec}} = \varepsilon_s + \varepsilon_h$, where ε_s is a smoothing parameter and ε_h is a hashing parameter. Overall, all these imperfections composed into a single global parameter which is the ε -security of the protocol, and given by $\varepsilon = p_{\text{ec}}\varepsilon_{\text{pe}} + \varepsilon_{\text{cor}} + \varepsilon_{\text{sec}}$ [13].

For a Gaussian-modulated coherent-state protocol [38, 39] with success probability p_{ec} and ε -security against collective (Gaussian) attacks [36], we may write the composable finite-size key rate [13, Appendix H]

$$R \geq r_n \left[R_m(\tau, \bar{n}') - \frac{\Delta_{\text{aep}}}{\sqrt{n}} + \frac{\Theta}{n} \right], \quad (60)$$

where

$$\Delta_{\text{aep}} := 4 \log_2 \left(2\sqrt{d} + 1 \right) \sqrt{\log_2 \frac{18}{p_{\text{ec}}^2 \varepsilon_s^4}}, \quad (61)$$

$$\Theta := \log_2 [p_{\text{ec}}(1 - \varepsilon_s^2/3)] + 2 \log_2 \sqrt{2} \varepsilon_h, \quad (62)$$

and d is the size of the alphabet after analog-to-digital conversion of the continuous variables of the parties.

For the specific case of the heterodyne protocol, one can extend the security to general coherent attacks [40]. This involves a suitable symmetrization of the data and performing $m_{\text{et}} = f_{\text{et}}n$ local energy tests, where they check if their local mean number of photons is $\lesssim \bar{n}_T + \mathcal{O}(m_{\text{et}}^{-1/2})$. For large enough m_{et} , this test is certainly passed and the parties achieve the rate [13, Appendix H]

$$R_{\text{gen}}^{\text{het}} \geq r_n \left[R_m^{\text{het}}(\tau, \bar{n}') - \frac{\Delta_{\text{aep}}}{\sqrt{n}} + \frac{\Theta - 2 \left[\log_2 \binom{K_n+4}{4} \right]}{n} \right], \quad (63)$$

where the number of key-generation pulses is

$$n = N - (m + m_{\text{et}}) = \frac{N - m}{1 + f_{\text{et}}}, \quad (64)$$

and we have set

$$K_n = \max \{1, 2n\bar{n}_T \Sigma_n\}, \quad (65)$$

$$\Sigma_n := \frac{1 + 2\sqrt{\frac{\ln(8/\varepsilon)}{2n}} + \frac{\ln(8/\varepsilon)}{n}}{1 - 2\sqrt{\frac{\ln(8/\varepsilon)}{2f_{\text{et}}n}}}. \quad (66)$$

Epsilon security becomes $\varepsilon' = K_n^4 \varepsilon / 50$ [40].

Note that, in a practical implementation, the parties exchange many pulses [41], which are split into $n_b \gg 1$ blocks of suitable size N for data processing; typically, $N = \mathcal{O}(10^6)$ or more. Assuming that the channel parameters are stable, one can write Eq. (60) for the generic

block, i.e., for $N = \mathcal{O}(10^6)$. The success probability p_{ec} provides the fraction of blocks that are successfully processed into key generation. Under conditions of stability, parameter estimation can be performed in one-go over the entire set of sacrificed pulses mn_b , so that the estimator in Eq. (56) is expected to be quite close to the actual value. However, if the channel is not stable, but still slowing varying with respect to the time-frame associated with a single block, then parameter estimation has to be done block-by-block and the final rate will be averaged over the blocks.

Another observation is about the potential use of a local local oscillator (instead of multiplexing the local oscillator with the signals). With this strategy, each signal pulse is transmitted before and after a reference pulse, which synchronizes the phases of the local oscillators at transmitter and receiver, also accounting for the Doppler effect associated with the motion of the satellite. Differently from the pilots, that are *randomly* interleaved with the signals, these reference pulses are regularly transmitted in alternation with the signals. If we use energies of the order of 1 nJ for each reference pulse (as for the pilots), the phase-matching is good with no relevant error introduced in the key rate. However, because of the use of extra pulses, this strategy will roughly halve the rate.

2. Fading and orbital dynamics

There are two basic reasons why the channel is not stable in satellite communications: One is the fading process affecting the transmissivity, even when the satellite is assumed to be at some fixed altitude and zenith angle; the other is the inevitable temporal variation of the zenith angle (and altitude) due to the specific orbit. We address both these issues below.

As already discussed, thanks to the pilots, the parties are able to monitor the instantaneous transmissivity τ of the channel and check the validity of the condition $\tau > \eta_{\text{th}}$ for each of the n signal pulses in a block of size N . In this way, they post-select np_{th} signal pulses, to which they associate the minimum value of the transmissivity η_{th} (so as to bound the worst-case scenario). The threshold transmissivity can be set to be a fraction of the maximum transmissivity η , i.e., $\eta_{\text{th}} = \phi\eta$ for some fixed $\phi < 1$. The value of η (and therefore that of η_{th}) can be considered to be constant over a single block if the latter results into a small orbital slice (which depends on the size of the block, the clock rate and the speed of the satellite). However, in general, the block may result into a larger orbital slice (e.g. with sensibly different zenith angles), so that the variation of η becomes non-trivial. In such a case, we assume the lowest value of η in the slice so as to bound the worst-case scenario.

We will better explore this strategy of orbital slicing afterwards. As a general study of feasibility we assume here that the slice associated with the block is smaller than the orbital section where the zenith angle is less than

1 radiant. We therefore compute the rate at 1 radiant as a lower bound for the actual rate that can be achieved. In such an approach, we implicitly assume that no quantum communication is performed at zenith angles outside the 1 radiant window, that we call the “good orbital section”.

Besides the transmissivity, the pilots also allow the parties to estimate the thermal number \bar{n} and to construct the worst-case estimator \bar{n}' . The thermal number is substantially independent from the fading process but may depend on the zenith angle (e.g., if we consider anisotropies in the brightness of the sky, or the partial presence of astronomical bodies in the receiver’s field of view). Depending on the orbit, it may be appropriate to assume weak dependence, in which case we can compute the estimator \bar{n}' in one-go over all blocks [i.e., by using $m \rightarrow mn_b$ in Eq. (56)], or we may have non-negligible dependence, in which case we compute \bar{n}' over each block [i.e., by using m in Eq. (56)] and then account for the different values when we average the key rate. In our study, we assume the simple case of a geometrically-constant noise (i.e., \bar{n} not depending on h and θ) but yet we compute its estimator \bar{n}' using m pulses of a single block (instead of mn_b). This approach provides a lower bound to the actual performance, and can be extended to the case of a geometrically-variable thermal noise by assuming the worst-case value of \bar{n} along the good orbital section.

With these arguments in mind, we modify the rates stated above. In particular, Eq. (60) takes the following expression [13, Appendix H]

$$R \geq \frac{np_{\text{th}}p_{\text{ec}}}{N} \left[R_m(\eta_{\text{th}}, \bar{n}') - \frac{\Delta_{\text{aep}}}{\sqrt{np_{\text{th}}}} + \frac{\Theta}{np_{\text{th}}} \right], \quad (67)$$

with a similar modification for the rate in Eq. (63). In fact, the latter simply becomes [13, Appendix H]

$$R_{\text{gen}}^{\text{het}} \geq \frac{np_{\text{th}}p_{\text{ec}}}{N} \left[R_m^{\text{het}}(\eta_{\text{th}}, \bar{n}') - \frac{\Delta_{\text{aep}}}{\sqrt{np_{\text{th}}}} + \frac{\Theta - 2 \left[\log_2 \left(\frac{K_n p_{\text{th}}}{4} + 4 \right) \right]}{np_{\text{th}}} \right], \quad (68)$$

with n and K_n given in Eqs. (64) and (65), and corresponding to an epsilon-security equal to $\varepsilon' = K_{np_{\text{th}}}^4 \varepsilon / 50$. We compute both these rates at $\theta = 1$ radiant.

We now have all the elements to study the 1-radiant composable key rates achievable by a pilot-guided post-selected heterodyne protocol at various satellite altitudes, for the configurations of night-time downlink/uplink and clear-day-time downlink. In particular, we choose the protocol parameters specified in Table III. The values of the input modulation μ (i.e., \bar{n}_T) and the threshold transmissivity ϕ (i.e., η_{th}) are implicitly optimized at each altitude. This is the case for rates against collective attacks (plotted for each configuration). For the study of the general attacks (only done in the best configuration of night-time downlink), we have made the sub-optimal choices of $\mu = 7.49$ and $\phi = 0.73$. Also note that the ep-

silon security ε' versus general attacks depends on the altitude; its maximum value shown in Table III is achieved for the minimum altitude of $h = 100$ km.

	Collective attacks	General attacks
N	10^8	10^8
n	$0.85 \times N$	$\simeq 4.47 \times 10^7$
m	$0.15 \times N$	$0.15 \times N$
d	2^5	2^5
β	0.96	0.96
p_{ec}	0.9	0.1
$\varepsilon_{\text{h,s},\dots}$	$2^{-33} \simeq 10^{-10}$	10^{-43}
w	$\simeq 6.34$	$\simeq 14.07$
ε	$\simeq 4.5 \times 10^{-10}$	(3.1×10^{-43})
ε'	—	$\lesssim 4.5 \times 10^{-11}$
f_{et}	—	0.9

TABLE III: Protocol parameters adopted with respect to collective attacks and general attacks.

Then, it is understood that we follow all the physical parameters and theoretical models considered so far, explicitly listed in Table IV. For the beam spot-size w_0 and the receiver aperture a_R , we consider the possible choices in Table V. The first setup in Table V corresponds to considering exactly the same physical conditions that we assumed for the calculations of the ultimate bounds, previously shown in Fig. 3. The other two setups offer a more generous hardware that allows us to improve the key rates in the various configurations.

Frequency	$\lambda = 800$ nm
Extinction	$\eta_{\text{atm}} \simeq [\eta_{\text{atm}}^{\text{zen}}(\infty)]^{\text{sec } 1} \simeq 0.94$
Pointing error	1 μ rad at the transmitter
Turbulence	night/day H-V model (App. C)
Background	Eqs. (39) and (40)
Efficiency	$\eta_{\text{eff}} = 0.4$
Filter	$\Delta\lambda = 1$ nm
Detection time	$\Delta t = 10$ ns
Field of view	$\Omega_{\text{fov}} = 10^{-10}$ sr

TABLE IV: Physical parameters and theoretical models.

	setup-1	setup-2	setup-3
w_0	20 cm	40 cm	40 cm
a_R	40 cm	1 m	2 m

TABLE V: Possible setups for spot size and receiver aperture.

In Fig. 4, we show the performances that are achievable in downlink assuming setup-1, which clearly improve when setup-2 is considered. However, we need to assume the more expensive setup-3 for enabling uplink

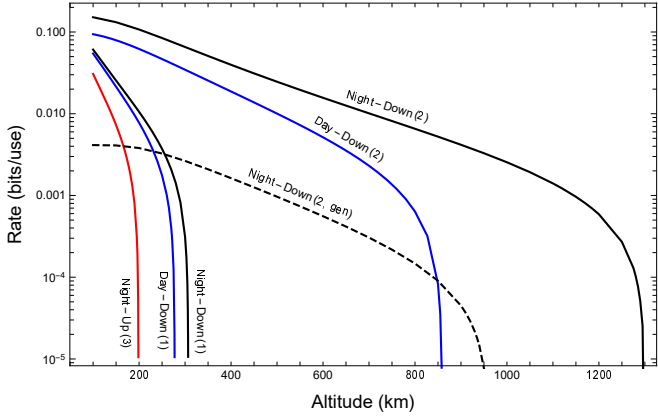


FIG. 4: 1-radian composable key rates (bits/use) achievable by a pilot-guided post-selected heterodyne protocol at various satellite altitudes h , for the configurations of night-time downlink (Night-Down), clear-day-time downlink (Day-Down) and night-time uplink (Night-Up). The value x in the brackets specifies the setup- x from Table V adopted in each case. In particular, the dashed line refers to night-time downlink with setup-2 against general attacks.

while keeping all the other parameters fixed. From the figure, we see that the LEO region is accessible by all configurations, even though with different requirements for the hardware.

3. Orbital slicing

The 1-radian key rates are pessimistic estimates of what we can actually achieve. For this reason, we now consider a more accurate treatment where we explicitly account for the fact that different blocks of data correspond to different slices of the orbit within the good section $\theta \leq 1$. In each slice we consider the minimum value for the transmissivity η , which is generally larger than the overall minimum value taken at 1 radian. Before presenting the improved rates, we need to make some preliminary considerations about an ideal modus operandi for the ground-satellite link.

In fact, we identify the following points:

- (i) The transit time of the satellite should allow the parties to distribute many quantum data points;
- (ii) There should be additional time for classical communication and data-processing, so that a secret key is generated before the end of the fly-by;
- (iii) There should be time for an encrypted private communication, exploiting part of the key already distributed.

To address these points, it is better to have a satellite able to reach small zenith angles. Clearly, an optimal solution is a satellite crossing the zenith point above

the ground station (zenith-crossing orbit). For simplicity, assume that its orbit is circular, with constant radius $R_S = R_E + h$ from the centre of the Earth. Examples of circular orbits are polar and near-polar sun-synchronous orbits. For a zenith-crossing circular orbit, the slant distance $z = z(R_S, \alpha)$ can be expressed as $z(R_S, \alpha) = \sqrt{R_E^2 + R_S^2 - 2R_E R_S \cos \alpha}$ in terms of $R_S = R_E + h$ and the orbital angle α (see also Eq. (A7) and Fig. 10).

Then, we may write the orbital period (in seconds)

$$T_S = 2\pi \sqrt{\frac{R_S^3}{\mu_G}}, \quad (69)$$

where $\mu_G = GM_E$ is the standard gravitational parameter, with $G = 6.674 \times 10^{-11} \text{ N m}^2 \text{ kg}^{-2}$ being the gravitational constant and $M_E \simeq 5.972 \times 10^{24} \text{ kg}$ the Earth's mass. As a result, the orbital angle α varies over time t according to the law

$$\alpha(t, h) = \frac{2\pi t}{T_S} = t \sqrt{\frac{\mu_G}{R_S^3}}, \quad (70)$$

where we have implicitly set $\alpha = 0$ (satellite at the zenith) for $t = 0$. Correspondingly, the time-varying zenith angle $\theta = \theta(t, h)$ can be computed from

$$\sin \theta = \frac{R_S \sin \alpha}{z(R_S, \alpha)}. \quad (71)$$

Note that here we associate a sign to θ (and α), so that a negative θ corresponds to the zenith angle with respect to a satellite which is arising from the “front” horizon and moving towards the zenith, while a positive θ corresponds to a satellite that has passed the zenith point and it is descending towards the “back” horizon.

We can divide the orbit in different sectors as depicted in Fig. 5. Assuming that the quantum communication occurs within 1 radian from the zenith (good section), we compute a corresponding *quantum transit time* t_Q . Within $|\theta| \leq \pi/2$, we may certainly invert $\theta = \theta(t, h)$ into $t = t(\theta, h)$. In fact, we may write

$$t(\theta, h) = \sqrt{\frac{(R_E + h)^3}{GM_E}} \arccos \left[\frac{R_E + z(h, \theta) \cos \theta}{R_E + h} \right], \quad (72)$$

where $z(h, \theta)$ is given in Eq. (1) and the initial condition is $t(0, h) = 0$. We then compute the quantum transit time $t_Q(h) = 2t(1, h)$ and the total transit time $t_T(h) := 2t(\pi/2, h)$ of the satellite from horizon to horizon. Their behaviours are plotted in Fig. 6.

As we can see, at 530 km, the total transit time is about 716 seconds, of which 200 seconds are within 1 radian. Assuming $t_Q \simeq 200$ and a typical clock of $C = 5 \text{ MHz}$, we have the quantum communication of $Ct_Q \simeq 10^9$ data points. Assuming blocks of $N = 10^8$ points, we have 10 blocks distributed within the 1-radian window of each passage. In other words, point (i) above can certainly be addressed.

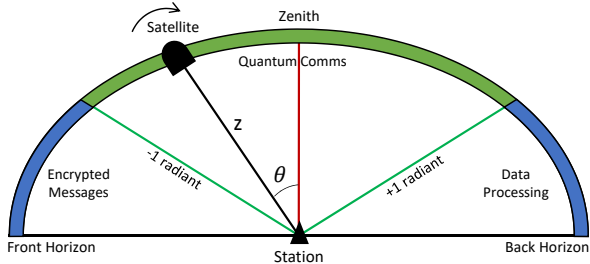


FIG. 5: Orbital sectors for a zenith-crossing circular orbit. Quantum communication occurs within the (green) good sector associated with the angular window $-1 \leq \theta \leq 1$ (where the angle is negative on the left, i.e., for a rising satellite). There is a transit time t_Q associated with this sector. Total transit time t_T is associated with the entire flyby from the front to the back horizon. The right blue sector $1 < \theta < \pi/2$ can be used for data processing and key generation. The left blue sector $-\pi/2 < \theta < 1$ can be used for encrypted communication using a previously generated key (e.g., the satellite may download the key exchanged with another station).

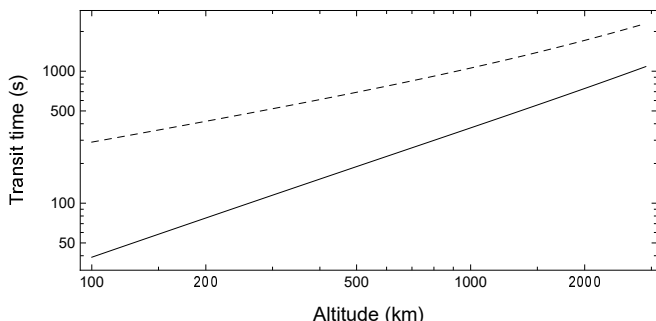


FIG. 6: Transit times (seconds) versus altitudes (kms) for a satellite passing through the zenith in a circular orbit. We plot the quantum transit time t_Q within the angle window $1 \leq \theta \leq 1$ (solid black) and the total transit time t_T from horizon to horizon (dashed black).

In order to address point (ii), we exploit the orbital sector after the 1-radian window (see Fig. 5) where a 530 km satellite spends $(t_T - t_Q)/2 \simeq 250$ seconds. These are more than sufficient for implementing the classical procedures of error correction and privacy amplification, e.g., using the high-speed methods of Refs. [42, 43]. Using optimal LDPC codes with a 1GHz GPU, the processing of 10^9 data points takes about 60 seconds [41, 44]. In particular, high speed is certainly achievable because of the relatively high signal-to-noise ratio. For a downlink from about 500 km, the total loss is less than 10 dB. Note that there is also a latency time in each communication with the satellite, which is of the order of 1.6 ms at that altitude. However, because all the procedures are essentially based on one-way CC, this effect only counts as an overall negligible delay.

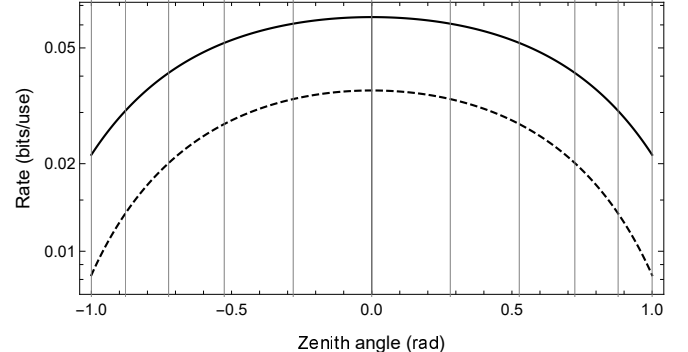


FIG. 7: Composable finite-size key rate R of Eq. (67) versus zenith angle θ in downlink from a satellite at $h = 530$ km along a zenith-crossing circular orbit. We plot the night-time (solid) and clear-day-time (dashed) performances. Parameters are specified in Table III for collective attacks, Table IV and Table V for setup-2. Other parameters are: $\mu = 9.28$ and $\phi = 0.73$ for night-time, and $\mu = 9.65$ and $\phi = 0.83$ for clear-day-time. Besides the rates we also show the angular lattice generated by the slices of Eq. (75).

Finally, there is the last point (iii) which is the time allocated for an encrypted communication between the satellite and the ground station. This session can be used for authentication and/or for downloading the key of another ground station via one-time pad. This step can be implemented during the first sector of the orbit, i.e., at zenith angles $-\pi/2 < \theta < -1$. In the basic scenario of Fig. 5, this phase is symmetric to that discussed above and it lasts $(t_T - t_Q)/2 \simeq 250$ seconds, clearly sufficient for the encrypted communication.

Let us now slice the good sector for quantum communication ($-1 \leq \theta \leq 1$) for a zenith-crossing circular orbit. Assume that n_{bks} blocks are transmitted during the flyby. Dividing the quantum transit time t_Q by n_{bks} , we get the time δt that is needed for each block to be transmitted. These time intervals identify corresponding angular slices $\{\theta_i, \theta_{i+1}\}$ along the orbit, that can be computed using Eqs. (70) and (71). For slice $i = 1, \dots, n_{\text{bks}}$ we consider the minimum value

$$R_i = \min_{\theta \in [\theta_i, \theta_{i+1}]} R(\theta), \quad (73)$$

where $R(\theta)$ is the θ -dependent key rate for the considered altitude. Thus, the average orbital rate is equal to

$$R_{\text{orb}} = \frac{1}{n_{\text{bks}}} \sum_{i=1}^{n_{\text{bks}}} \max\{0, R_i\} \geq R_{1\text{-rad}}, \quad (74)$$

where the bound $R_{1\text{-rad}} := \max\{0, R(\theta = \pm 1)\}$ is the rate associated with the border values (considered in the previous subsection and Fig. 4).

In our numerical investigation with a zenith-crossing circular orbit at $h = 530$ km, the quantum transit time is about 200 seconds. Therefore we may consider $n_{\text{bks}} = 10$ blocks, where each block of size $N = 10^8$ corresponds to

a transmission time of $\delta t = 20$ seconds for a $C = 5$ MHz clock. This configuration identifies the angular slices:

$$\begin{aligned} \{\theta_i, \theta_{i+1}\} \simeq & \{-1, -0.88\}, \{-0.88, -0.72\}, \\ & \{-0.72, -0.53\}, \{-0.53, -0.28\}, \\ & \{-0.28, 0\}, \{0, 0.28\}, \{0.28, 0.53\}, \\ & \{0.53, 0.72\}, \{0.72, 0.88\}, \{0.88, 1\}. \end{aligned} \quad (75)$$

The lattice is shown in Fig. 7 together with the rate $R(\theta)$ of Eq. (67) for night-time and clear-day-time downlink. For this rate we have assumed the protocol parameters in Table III for collective attacks, the physical parameters in Table IV together with the setup-2 from Table V. The values for the modulation μ and the threshold ϕ are chosen in such a way to maximize the lowest rate in the ensemble $\{R_i\}_{i=1}^{n_{\text{bks}}}$. For a circular orbit, it is clear that the lowest rate is the one achieved at the larger zenith angle (in particular, if all the good sector is filled by the slices, then the values of μ and ϕ are chosen from the optimization of $R_{1\text{-rad}}$). Thus, in the figure, we have chosen $\mu = 9.28$ and $\phi = 0.73$ for night-time, and $\mu = 9.65$ and $\phi = 0.83$ for clear-day-time.

Using Eqs. (67) and (75) in Eq. (74), we compute the average orbital rate for downlink, which is equal to

$$R_{\text{orb}}^{\text{down}} \simeq \begin{cases} 4.1 \times 10^{-2} \text{ bits/use (night-time)} \\ 2 \times 10^{-2} \text{ bits/use (clar-day-time).} \end{cases} \quad (76)$$

By definition, “per use” means per use of the quantum communication channel, occurring within 1 radiant. When we plug a clock $C = 5$ MHz, we have a rate of $R_{\text{orb}}^{\text{down}} \simeq 205$ kbit/s during night time, and $R_{\text{orb}}^{\text{down}} \simeq 102$ kbit/s during clear day time. Accounting for the time for quantum communication (200 s), each night-time zenith-crossing passage distributes $\simeq 4.1 \times 10^7$ secret bits, while a day-time zenith-crossing passage distributes $\simeq 2 \times 10^7$ secret bits. Considering that, within 24 hours, there will be other non-zenith-crossing passages (exploitable for QKD), the above estimates lowerbound the number of bits that can be distributed per day via night- and day-time operation.

Let us now consider uplink during night time. As we can see from Fig. 4, the 1-radian rate is positive at reasonable LEO altitudes but clearly requires a more demanding setup compared to those for downlink. As we have already discussed, the main reason for this inferior performance is the non-trivial effect of atmospheric turbulence in this configuration. We start from the rate $R(\theta)$ of Eq. (67) specified for night-time uplink and assuming the protocol parameters in Table III for collective attacks, the physical parameters in Table IV and setup-3 from Table V. For our numerical investigation, we consider a satellite at $h = 155$ km. Because of the lower altitude, we have a total transit time of just $t_T \simeq 364$ s and a quantum transit time of $t_Q \simeq 60$ s. The latter allows the parties to distribute 3 blocks of size 10^8 with a clock of $C = 5$ MHz. The orbital slices associated to

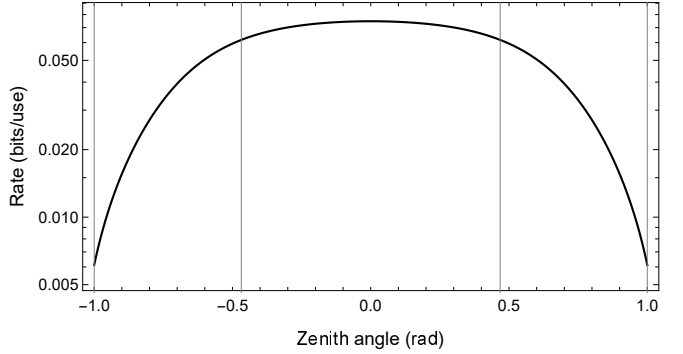


FIG. 8: Composable finite-size key rate R of Eq. (67) versus zenith angle θ for night-time uplink to a satellite at $h = 155$ km along a zenith-crossing circular orbit. Parameters are specified in Table III for collective attacks, Table IV and Table V relative to setup-3. Other parameters are $\mu = 7$ and $\phi = 0.68$. We also show the three angular slices specified by Eq. (77).

each 20 s-long block are given by

$$\{\theta_i, \theta_{i+1}\} \simeq \{-1, -0.468\}, \{-0.468, 0.468\}, \{0.468, 1\}. \quad (77)$$

Both the rate $R(\theta)$ and the slices are shown in Fig. 8.

Using Eqs. (67) and (77) in Eq. (74), we compute the average orbital rate for night-time uplink, which is equal to

$$R_{\text{orb}}^{\text{up}} \simeq 2.46 \times 10^{-2} \text{ bits/use.} \quad (78)$$

At 5 MHz this rate corresponds to about 123 kbit/s. Then, accounting for quantum transit time of 60 s, we have that each night-time zenith-crossing passage distributes $\simeq 7.39 \times 10^6$ secret bits in uplink.

H. Satellites versus ground-based repeaters

We can show how satellite quantum communications are able to provide a non-trivial advantage with respect to the use of ground networks. A simple example of circular orbit is clearly a polar orbit, i.e., with orbital inclination $\iota = 90^\circ$. However, a more practical scenario considered here is that of a near-polar satellite in sun-synchronous orbit (which is almost circular). This type of orbit guarantees that the satellite passes over any point on Earth’s surface at the same local mean solar time. This clearly implies the possibility of stable conditions for night-time or day-time operation so that, for example, the ground-satellite quantum communication may always occur at roughly the same time of the night or the day (at reasonable low latitudes).

For a sun-synchronous satellite at altitude h , the orbital inclination is given by

$$\iota = \frac{360}{2\pi} \arccos \left[- \left(\frac{R_E + h}{12352} \right)^{7/2} \right], \quad (79)$$

where $h \leq 5980$ is expressed in km. At $h = 530$ km, this corresponds to $\iota \simeq 97.5^\circ$. Because the orbital period is $T_S \simeq 95$ minutes, the satellite performs 15 orbits a day, before returning above the initial point. Note that the Micius satellite is sun-synchronous with $\iota \simeq 97.4^\circ$ and an altitude between 488 and 584 km. At $h = 155$ km, we have $\iota \simeq 96.1^\circ$, $T_S \simeq 87$ minutes and 16 orbits a day.

Assume that two ground stations are along the orbital path, so that the satellite crosses both their zenith positions, which happens once per day. We assume the worst-case scenario in which the stations interact with the satellite only during the sections of the orbit where the zenith positions are crossed (of course this assumption can be relaxed and the ground stations could also use other passages that are not zenith-crossing). Also assume that the stations are in similar operational conditions, so that we can simultaneously adopt the results for night time or day time for both of them. Finally, assume that the satellite may have the option to communicate with two stations simultaneously (e.g., using two quantum transmitters or receivers); this addresses the case where the stations are close so that the satellite appears within their 1-radiant angular window roughly at the same time (clearly this is not the case for very distant ground stations).

Start with the satellite at the zenith of the first station ($t = 0$) and assume that it reaches the zenith of the second station after time Δt . For $\Delta t \leq T_S/2$, the distance between the two stations is equal to

$$d_{\text{st}} = \alpha(\Delta t, h) R_E = \frac{2\pi\Delta t R_E}{T_S} \in [0, \pi R_E], \quad (80)$$

where we have used Eq. (70) and accounted for Earth's curvature. Then, consider that the two stations are also connected by an optical fiber with standard loss-rate of $\alpha_{\text{fib}} = 0.2 \text{ dB/km}$, so that we have a total fiber transmissivity of $\eta_{\text{fib}} = 10^{-\alpha_{\text{fib}} d_{\text{st}}/10}$. The maximum fiber-based repeater-less rate (bits per use) is given by the PLOB bound $R_{\text{fib}} = -\log_2(1 - \eta_{\text{fib}})$ [12]. Multiplying by the clock $C = 5 \text{ MHz}$ and the number of seconds in one day $\#_{\text{day}} \simeq 8.6 \times 10^4$, we may compute the maximum number of secret bits that can be distributed in one day $CR_{\text{fib}} \#_{\text{day}}$ as a function of the station-to-station ground distance. We also assume the situation where a number $N_{\text{rep}} \geq 1$ of ideal repeaters are inserted along the fiber line, so that we have the fiber-based rate becomes $R_{\text{fib}}^{\text{rep}} = -\log_2(1 - \sqrt[N_{\text{rep}}]{\eta_{\text{fib}}})$ [15]. We have a corresponding number of secret bits $CR_{\text{fib}}^{\text{rep}} \#_{\text{day}}$ per day.

In Fig. 9, we consider the maximum number of secret bits per day (versus ground distance) that can be distributed by a repeaterless fiber link between the stations and also by fiber-links assisted by ideal quantum repeaters. Assuming the same clock, we compare these ground-based performances with the secret-bits per day that can be distributed by using a satellite moving between the two stations, the latter operating in the same way with respect to the satellite, i.e., via night-time/day-time downlink [Eq. (76)] and night-time uplink [Eq. (78)].

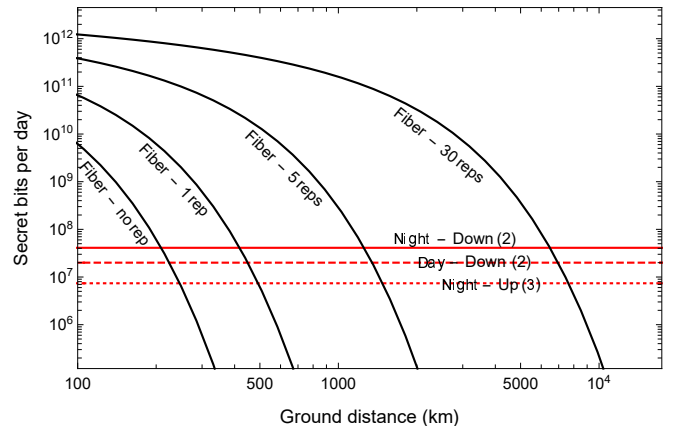


FIG. 9: Secret bits per day versus ground distance (km) between two stations, assuming a clock of 5 MHz. We consider the maximum performances achievable by a repeaterless fiber-connection (PLOB bound) and repeater-based fiber-connections assisted by 1, 5 and 30 ideal quantum repeaters (solid lines). These are compared with the constant performances achievable by connecting the two ground stations via a near-polar sun-synchronous satellite. We consider $h = 530$ km for night-/clear-day-time downlink and we assume all the parameters leading to Eq. (76), in particular setup-2 of Table V. For night-time uplink we consider $h = 155$ km, together with all parameters leading to Eq. (78), in particular setup-3 of Table V.

We can see how a satellite can easily beat the fiber-based repeaterless bound when the stations are separated by more than 200 km, and how it can achieve the same rate of 30 ideal quantum repeaters when the station-to-station ground separation is about 6500 km.

III. CONCLUSIONS

In this work we have established the ultimate limits and the practical rates that can be achieved in secure quantum communications with satellites, assuming various configurations (downlink/uplink) and operation settings (night- or day-time). While our study is based on ideas and tools developed in Ref. [13] for free-space quantum communications, it also required a number of non-trivial generalizations in order to account for the slant propagation at variable altitudes and beyond the atmosphere. As a matter of fact, the underlying physical models for atmospheric turbulence and background noise have crucial differences with respect to the models adopted for free-space communications on the ground.

We have started by establishing information-theoretic upper limits to the maximum number of secret bits (and ebits) that can be achieved per use of the satellite link in all scenarios. Our analysis has gradually considered all effects due to diffraction, extinction, limited efficiency, pointing error, atmospheric turbulence and background noise.

In uplink, turbulence is very important because it affects the beam close to the transmitter where the spot size is small. In this case, both pointing error and turbulence effects must be accounted for. By contrast, in downlink, the spot size is already very large when it enters the atmosphere, compared to the typical size of the turbulent eddies. For this reason, turbulence is negligible and the only relevant effect is the pointing error. A further asymmetry is introduced by the background noise induced by sky brightness and planetary albedos (Moon and Earth). In particular, the use of day-time uplink appears to be restricted to short ranges, i.e., to sub-LEO satellites for the specific parameters explored.

For this reason, we have focused our attention on the more advantageous configurations of night-time downlink, night-time uplink and clear-day-time downlink. For all these settings we have studied the numerical behavior of the ultimate key rates when the satellite is at the zenith position or at 1 radian from the zenith, showing that a large range of altitudes are possible for secure key generation (and entanglement distribution) when we adopt optimal protocols. For the same configurations, we have then studied secret key rates that are achievable in prac-

tice by accounting for finite-size effects and composable security. The use of a pilot-guided post-selected heterodyne protocol combined with a careful consideration for the orbital dynamics allows the implementation of CV-QKD between station and satellite in all the configurations (night-time downlink/uplink, clear-day-time downlink). It is interesting that night-time uplink represents indeed a viable option for secure quantum communications, whereas only the setting of night-time downlink has been considered in other works (e.g., see Ref. [76]).

Finally, we have shown that a sun-synchronous satellite, exchanging keys with ground stations, is able to distribute more secret bits per day than a direct fiber-connection between the stations, even if the latter communicate at the ultimate PLOB bound. Remarkably, the satellite is also able to outperform a chain of many ideal quantum repeaters operating between the remote stations. These results are obtained when the distance between the remote stations surpasses certain thresholds, which depend on the hardware available for the satellite together with the adopted configuration (downlink/uplink) and operational setting (night/day time).

[1] S. Pirandola, U. L. Andersen, L. Banchi, M. Berta, D. Bunandar, R. Colbeck, D. Englund, T. Gehring, C. Lupo, C. Ottaviani, J. Pereira, M. Razavi, J. S. Shaari, M. Tomamichel, V. C. Usenko, G. Vallone, P. Villoresi, and P. Wallden, *Advances in Quantum Cryptography*, arXiv:1906.01645 (2019).

[2] G. Vallone, D. Bacco, D. Dequal, S. Gaiarin, V. Luceri, G. Bianco, and P. Villoresi, *Experimental Satellite Quantum Communications*, Phys. Rev. Lett. **115**, 040502 (2015).

[3] S.-K. Liao, W.-Q. Cai, W.-Y. Liu, L. Zhang, Y. Li, J.-G. Ren, J. Yin, Q. Shen, Y. Cao, and Z.-P. Li et al., *Satellite-to-ground quantum key distribution*, Nature **549**, 43 (2017).

[4] S.-K. Liao, W.-Q. Cai, J. Handsteiner, B. Liu, J. Yin, L. Zhang, D. Rauch, M. Fink, J.-G. Ren, and W.-Y. Liu et al., *Satellite-Relayed Intercontinental Quantum Network*, Phys. Rev. Lett. **120**, 030501 (2018).

[5] J. Yin, Y. Cao, Y.-H. Li, S.-K. Liao, L. Zhang, J.-G. Ren, W.-Q. Cai, W.-Y. Liu, B. Li, and H. Dai et al., *Satellite-based entanglement distribution over 1200 kilometers*, Science **356**, 1140 (2017).

[6] J. Yin, Y. Cao, Y. H. Li, J. G. Ren, S. K. Liao, L. Zhang, W. Q. Cai, W. Y. Liu, B. Li, and H. Dai et al., *Satellite-to-Ground Entanglement-Based Quantum Key Distribution*, Phys. Rev. Lett. **119**, 200501 (2017).

[7] J. Yin, Y.-H. Li, S.-K. Liao, M. Yang, Y. Cao, L. Zhang, J.-G. Ren, W.-Q. Cai, W.-Y. Liu, S.-L. Li, et al., *Entanglement-based secure quantum cryptography over 1,120 kilometres*, Nature **582**, 501 (2020).

[8] J. G. Ren, P. Xu, H. L. Yong, L. Zhang, S. K. Liao, J. Yin, W. Y. Liu, W. Q. Cai, M. Yang, and L. Li et al., *Ground-to-satellite quantum teleportation*, Nature **549**, 70 (2017).

[9] S. K. Liao, J. Lin, J. G. Ren, W. Y. Liu, J. Qiang, J. Yin, Y. Li, Q. Shen, L. Zhang, and X. F. Liang et al., *Space-to-Ground Quantum Key Distribution Using a Small-Sized Payload on Tiangong-2 Space Lab*, Chin. Phys. Lett. **34**, 090302 (2017).

[10] H. Takenaka, A. Carrasco-Casado, M. Fujiwara, M. Kitamura, M. Sasaki, and M. Toyoshima, *Satellite-to-ground quantum-limited communication using a 50-kgclass microsatellite*, Nat. Photon. **11**, 502 (2017).

[11] A. Villar, A. Lohrmann, X. Bai, T. Vergoossen, R. Bedington, C. Perumangatt, H. Y. Lim, T. Islam, A. Reewhana, Z. Tang, et al., *Entanglement demonstration on board a nano-satellite*, Optica **7**, 734 (2020).

[12] S. Pirandola, R. Laurenza, C. Ottaviani, and L. Banchi, *Fundamental limits of repeaterless quantum communications*, Nat. Commun. **8**, 15043 (2017). See also arXiv:1510.08863 (2015).

[13] S. Pirandola, *Limits and Security of Free-Space Quantum Communications*, arXiv:2010.04168 (2020).

[14] C. Weedbrook, S. Pirandola, R. García-Patrón, N. J. Cerf, T. C. Ralph, J. H. Shapiro, and S. Lloyd, *Gaussian Quantum Information*, Rev. Mod. Phys. **84**, 621 (2012).

[15] S. Pirandola, *End-to-end capacities of a quantum communication network*, Commun. Phys. **2**, 51 (2019). See also arXiv:1601.00966 (2016).

[16] O. Svelto, *Principles of Lasers*, 5th edn. (Springer, New York 2010).

[17] L. C. Andrews, W. B. Miller, and J. C. Ricklin, *Geometrical representation of Gaussian beams propagating through complex paraxial optical systems*, Appl. Opt. **32**, 5918-5929 (1993).

[18] L. C. Andrews, W. B. Miller, and J. C. Ricklin, *Spatial coherence of a Gaussian-beam wave in weak and strong optical turbulence*, J. Opt. Soc. Am. A **11**, 1653-1660

(1994).

[19] A. Siegman, *Lasers* (University Science Books, 1986).

[20] C. F. Bohren and D. R. Huffman, *Absorption and scattering of light by small particles* (John Wiley & Sons, 2008).

[21] D. Vasylyev, W. Vogel, and F. Moll, *Satellite-mediated quantum atmospheric links*, Phys. Rev. A **99**, 053830 (2019).

[22] C. Liorni, H. Kampermann, and D. Bruß, *Satellite-based links for quantum key distribution: beam effects and weather dependence*, New J. Phys. **21**, 093055 (2019).

[23] R. Esposito, *Power Scintillations Due to the Wandering of the Laser Beam*, Proc. IEEE **55**, 1533-1534 (1967).

[24] D. Fried, *Statistics of laser beam fade induced by pointing jitter*, App. Opt. **12**, 422-423 (1973).

[25] P. Titterton, *Power reduction and fluctuations caused by narrow laser beam motion in the far field*, Appl. Opt. **12**, 423-425 (1973).

[26] D. Yu. Vasylyev, A. A. Semenov, W. Vogel, *Toward Global Quantum Communication: Beam Wandering Preserves Nonclassicality*, Phys. Rev. Lett. **108**, 220501 (2012).

[27] R. L. Fante, *Electromagnetic Beam Propagation in Turbulent Media*, Proc. IEEE **63**, 1669 (1975).

[28] J.-P. Bourgoin, E. Meyer-Scott, B. L. Higgins, B. Helou, C. Erven, H. Hübel, B. Kumar, D. Hudson, I. D’Souza, R. Girard, R. Laflamme, and T. Jennewein, *A comprehensive design and performance analysis of low Earth orbit satellite quantum communication*, New J. Phys. **15**, 023006 (2013).

[29] R. E. Hufnagel and N. R. Stanley, *Modulation transfer function associated with image transmission through turbulent media*, J. Opt. Soc. Am. **54**, 52-61 (1964).

[30] G. C. Valley, *Isoplanatic degradation of tilt correction and short-term imaging systems*, Appl. Opt. **19**, 574-577 (1980).

[31] L. C. Andrews and R. L. Phillips, *Laser Beam Propagation Through Random Medium*, 2nd edn. (SPIE, Bellingham, 2005).

[32] R.L. Fante, *Electromagnetic beam propagation in turbulent media: An update*, Proc. IEEE **68**, 1424 (1980).

[33] H. Yura, *Short term average optical-beam spread in a turbulent medium*, J. Opt. Soc. Am. **63**, 567-572 (1973).

[34] J. Dowling and P. Livingston, *Behavior of focused beams in atmospheric turbulence: Measurements and comments on the theory*, J. Opt. Soc. Am. **63**, 846-858 (1973).

[35] S. Pirandola, R. García-Patrón, S. L. Braunstein, and S. Lloyd, *Direct and reverse secret-key capacities of a quantum channel*, Phys. Rev. Lett. **102**, 050503 (2009).

[36] S. Pirandola, S. L. Braunstein, S. Lloyd, *Characterization of collective Gaussian attacks and security of coherent-state quantum cryptography*, Phys. Rev. Lett. **101**, 200504 (2008).

[37] Note that, under the hypothesis that the environmental noise is assumed to be trusted, then Eq. (44) and (47) do not apply, but the optimal QKD rate is still bounded by the pure-loss bound in Eq. (34).

[38] F. Grosshans and P. Grangier, *Continuous Variable Quantum Cryptography Using Coherent States*, Phys. Rev. Lett. **88**, 057902 (2002).

[39] C. Weedbrook, A. M. Lance, W. P. Bowen, T. Symul, T. C. Ralph, and P. K. Lam, *Quantum Cryptography Without Switching*, Phys. Rev. Lett. **93**, 170504 (2004).

[40] A. Leverrier, *Security of Continuous-Variable Quantum Key Distribution via a Gaussian de Finetti Reduction*, Phys. Rev. Lett. **118**, 200501 (2017).

[41] Y.-C. Zhang, Z. Chen, S. Pirandola, X. Wang, C. Zhou, B. Chu, Y. Zhao, B. Xu, S. Yu, and H. Guo, *Long-Distance Continuous-Variable Quantum Key Distribution over 202.81 km of Fiber*, Phys. Rev. Lett. **125**, 010502 (2020).

[42] X. Wang, Y. Zhang, S. Yu, and H. Guo, *High speed error correction for continuous-variable quantum key distribution with multi-edge type LDPC code*, Sci. Rep. **8**, 10543 (2018).

[43] X. Wang, Y. Zhang, S. Yu, and H. Guo, *High-speed implementation of length-compatible privacy amplification in continuous-variable quantum key distribution*, IEEE Photon. Journal **10**, 7600309 (2018).

[44] Yichen Zhang, private communication.

[45] A. R. Thompson, J. M. Moran, and G. W. Jr. Swenson, *Interferometry and Synthesis in Radio Astronomy* (3rd ed., Springer Open, 2017).

[46] V. Klyatskin and A. Kon, *On the displacement of spatially bounded light beams in a turbulent medium in the Markovian random-process approximation*, Radiophys. Quantum Electron **15**, 1056-1061 (1972).

[47] H. Kaushal, V. K. Jain, and S. Kar, *Free Space Optical Communication* (Springer, New York, 2017).

[48] D. H. Tofsted, S. G. O’Brien, and G. T. Vaucher, *An atmospheric turbulence profile model for use in army war gaming applications I*, Technical Report ARL-TR-3748 US Army Research Laboratory (2006).

[49] D. Vasylyev, A. A. Semenov, W. Vogel, K. Günthner, A. Thurn, Ö. Bayraktar, and Ch. Marquardt, *Free-space quantum links under diverse weather conditions*, Phys. Rev. A **96**, 043856 (2017).

[50] T. W. VanZandt, J. L. Green, K. S. Gage, and W. L. Clark, *Vertical profiles of refractivity turbulence structure constant: Comparison of observations by the Sunset Radar with a new theoretical model*, Radio Sci. **5**, 819 (1978).

[51] E. M. Dewan, R. E. Good, R. Beland, and J. Brown, *A model for C_n^2 (optical turbulence) profiles using radiosonde data*, Environmental Research Papers, Report No. **1121**, PL-TR-93-2043, 1993 (unpublished).

[52] D. L. Walters and K. E. Kunkel, *Atmospheric modulation transfer function for desert and mountain locations: The atmospheric effects on r_0* , J. Opt. Soc. Am. **71**, 397 (1981).

[53] R. Frehlich, R. Sharman, F. Vandenbergh, W. Yu, Y. Liu, and J. Knievel, *Estimates of C_n^2 from numerical weather prediction model output and comparison with thermosonde data*, J. Appl. Meteor. Climatol. **49**, 1742 (2010).

[54] D. L. Fried, *Limiting Resolution Looking Down Through the Atmosphere*, J. Opt. Soc. Am. **56**, 1380-1384 (1966).

[55] A. K. Majumdar and J. C. Ricklin, *Free-Space Laser Communications* (Springer New York, 2008).

[56] J. W. Goodman, *Statistical Optics* (John Wiley & Sons, Inc., 1985).

[57] L. C. Andrews, R. L. Phillips, and P. T. Yu, *Optical scintillations and fade statistics for a satellite-communication system*, Appl. Opt. **34**, 7742-7751 (1995).

[58] P. A. Lightsey, *Scintillation in ground-to-space and retroreflected laser beams*, Opt. Eng. **33**, 2535-2543 (1994).

- [59] A. M. Prokhorov, F. V. Bunkin, K. S. Gochelashvily, and V. I. Shishov, *Laser irradiance propagation in turbulent media*, Proc. IEEE **63**, 790-809 (1975).
- [60] L. C. Andrews, W. B. Miller, and J. C. Ricklin, *Spatial coherence of a Gaussian-beam wave in weak and strong optical turbulence*, J. Opt. Soc. Am. A **11**, 1653-1660 (1994).
- [61] L. C. Andrews, R. L. Phillips, and C. Y. Young, *Scintillation model for a satellite communication link at large zenith angles*, Optical Engineering **39**(12), (2000).
- [62] S. M. Rytov, *Diffraction of light by ultrasonic waves*, Izvestiya Akademii Nauk SSSR, Seriya Fizicheskaya (Bulletin of the Academy of Sciences of the USSR, Physical Series) **2**, 223-259 (1937).
- [63] A. N. Kolmogorov, *The local structure of turbulence in an incompressible viscous fluid for very large Reynolds numbers*, C. R. (Dokl) Acad. Sci. U.S.S.R. **30**, 301-305 (1941).
- [64] H. T. Yura and W. G. McKinley, *Optical scintillation statistics for IR ground-to-space laser communication systems*, Appl. Opt. **22**, 3353-3358 (1983).
- [65] B. Béland, *The Infrared and Electro-Optical System Handbook*, vol. 2 (SPIE Press, 1993).
- [66] J. Poirier and D. Korff, *Beam spreading in a turbulent medium*, J. Opt. Soc. Am. **62**, 893-898 (1972).
- [67] F. Bunkin and K. Gochelashvily, *Spreading of a light beam in a turbulent medium*, Radiophys. Quantum Electron. **13**, 811-821 (1970).
- [68] F. Dios, J. A. Rubio, A. Rodríguez, and A. Comerón, *Scintillation and beam-wander analysis in an optical ground station-satellite uplink*, Appl. Opt. **43**, 3866-3873 (2004).
- [69] A. Belmonte, *Feasibility study for the simulation of beam propagation: consideration of coherent lidar performance*, Appl. Opt. **39**, 5426-5445 (2000).
- [70] J. H. Lambert, *Photometria, sive de Mensura et gradibus luminis, colorum et umbrae* (1760).
- [71] F. L. Pedrotti and L. S. Pedrotti, *Introduction to Optics* (Prentice Hall, 1993).
- [72] C. Bonato, A. Tomaello, V. Da Depo, G. Naletto, and P. Villoresi, *Feasibility of satellite quantum key distribution*, New J. Phys **11**, 045017 (2009).
- [73] E.-L. Miao, Z.-F. Han, S.-S. Gong, T. Zhang, D.-S. Diao, and G.-C. Guo, *Background noise of satellite-to-ground quantum key distribution*, New J. Phys. **7**, 215 (2005).
- [74] Ch. Leinert, S. Bowyer, L. K. Haikala, M. S. Hanner, M. G. Hauser, A.-Ch. Levasseur-Regourd, I. Mann, K. Mattila, W. T. Reach, W. Schlosser, H. J. Staude, G. N. Toller, J. L. Weiland, J. L. Weinberg and A. N. Witt, *The 1997 reference of diffuse night sky brightness*, Astron. Astrophys. Suppl. Ser. **127**, 1-99 (1998).
- [75] V. Hansen, *Spectral Distribution of Solar Radiation on Clear Days: A Comparison Between Measurements and Model Estimates*, Journal of Climate and Applied Meteorology **23**, 772-780 (1984).
- [76] D. Dequal, L. T. Vidarte, V. R. Rodriguez, G. Vallone, P. Villoresi, A. Leverrier, and E. Diamanti, *Feasibility of satellite-to-ground continuous-variable quantum key distribution*, arXiv:2002.02002 (2020).

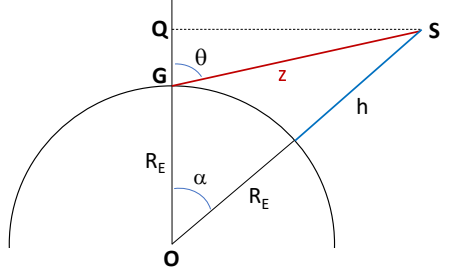


FIG. 10: Basic geometry for satellite communications. A satellite (S) is at slant distance z from a sea-level ground station (G). The satellite is at zenith angle θ and altitude h over the Earth's surface. Clearly, $z = h$ only at the zenith ($\theta = 0$). The satellite is also at the orbital angle α and orbital radius $R_S = h + R_E$, where R_E is the radius of the Earth. Note that $\overline{OQ} = R_E + \overline{QG} = \overline{OS} \cos \alpha$ leads to (1) $R_E + z \cos \theta = R_S \cos \alpha$. Now, from \overline{QS} have: (2) $z \sin \theta = R_S \sin \alpha$. By taking the squared in (1) and (2) and using $\cos^2 \alpha = 1 - \sin^2 \alpha$, we derive $h^2 + 2R_E h - z(z + 2R_E \cos \theta) = 0$ whose positive solution gives Eq. (A1). In a similar way, one can use $\cos^2 \theta = 1 - \sin^2 \theta$ and derive Eq. (A7).

Appendix A: Basic geometry for satellite communications

Here we discuss some geometrical elements about communications with satellites. The slant distance z between a sea-level ground station and a satellite can be connected with other two important parameters. The first one is the (positive) zenith angle θ which is defined as the angle between the vertical direction (zenith) and the pointing direction from the ground station to the satellite. The second one is the altitude h of the satellite, which is defined as the distance from the satellite to the ground (sea-level) orthogonally to the surface of the Earth. Slant distance z , altitude h , and (positive) zenith angle $\theta \in [-\pi/2, \pi/2]$ can be easily connected by means of simple trigonometric observations.

It is easy to express the altitude h as a function of z and θ . A simple trigonometric calculus provides

$$h(z, \theta) = \sqrt{R_E^2 + z^2 + 2zR_E \cos \theta - R_E}, \quad (\text{A1})$$

where $R_E \simeq 6371$ km is the approximate radius of the Earth (see Fig. 10). In particular, at small angles $\theta \simeq 0$, we can write the simplified “flat-Earth” approximation

$$h(z, \theta) \simeq z \cos \theta + \mathcal{O}(\theta^3), \quad \theta_z := \theta \sqrt{\frac{R_E}{R_E + z}}. \quad (\text{A2})$$

For $\theta \leq 1$ and relatively small h (of the order of the atmospheric thickness, i.e., 20 km), one finds that $h \simeq z \cos \theta$ and $z \simeq h \sec \theta$ represent excellent approximations.

It is easy to see that Eq. (A1) can be inverted into

$$\cos \theta = \frac{h}{z} + \frac{h^2 - z^2}{2zR_E}, \quad (\text{A3})$$

which gives the zenith angle θ in terms of z and h (see also Ref. [45, Ch. 13]). Similarly, the slant range z can be expressed as a simple function of h and θ , i.e., we may write the slant distance functional (see also Ref. [21])

$$z(h, \theta) = \sqrt{h^2 + 2hR_E + R_E^2 \cos^2 \theta} - R_E \cos \theta. \quad (\text{A4})$$

Note that $z(h, \theta) \leq h \sec \theta$ for any h and $\theta \in [0, \pi/2]$.

It is easy to verify that the previous formulas can immediately be generalized to the scenario where the ground station is located at some non-zero altitude h_0 . Setting $R_G := R_E + h_0$ and $R_S = R_E + h$, we may in fact write

$$h(z, \theta) = \sqrt{R_G^2 + z^2 + 2zR_G \cos \theta} - R_E, \quad (\text{A5})$$

$$z(h, \theta) = \sqrt{R_S^2 + R_G^2(\cos^2 \theta - 1)} - R_G \cos \theta. \quad (\text{A6})$$

Another parametrization is in terms of orbital radius R_S and the orbital angle α , i.e., the angle between the position of the ground station and the position of the satellite as seen from the centre of the Earth. It is immediate to see that

$$z(R_S, \alpha) = \sqrt{R_E^2 + R_S^2 - 2R_E R_S \cos \alpha}. \quad (\text{A7})$$

This parametrization is useful for circular orbits, where R_S is constant. In this case, we can write $\alpha = 2\pi t/T_S$ where t is time and T_S is the orbital period, i.e., the time needed for a complete revolution around the Earth.

Appendix B: Refraction effects

In a more refined description, we need to consider atmospheric refraction. Assuming the atmosphere to be modeled as a set of thin uniform slabs provides the same result of an atmosphere modeled as a single uniform slab with surface refractive index n_0 [45, Ch. 13, Fig. 13.4]. Therefore, atmospheric refraction creates an apparent zenith angle θ_{app} satisfying Snell's law

$$\sin \theta_{\text{app}} = n_0^{-1} \sin \theta, \quad (\text{B1})$$

where $n_0 \simeq 1.00027$ is the surface value of the refractive index. We see that the angle of refraction $\Delta\theta := \theta - \theta_{\text{app}}$ exceeds one degree when the satellite is at the horizon, where $\theta = \pi/2$ corresponds to $\theta_{\text{app}}^{\max} \simeq 1.548$ ($\simeq 88.7^\circ$). Besides the apparent angle, refraction also increases the optical path by an elongation factor $\varepsilon_{\text{elo}} = \varepsilon_{\text{elo}}(\theta_{\text{app}})$.

Replacing $\theta = \theta(\theta_{\text{app}}) := \arcsin(n_0 \sin \theta_{\text{app}})$ in $z(h, \theta)$ and multiplying by ε_{elo} , one gets the refracted slant range

$$z_{\text{ref}}(h, \theta_{\text{app}}) = \varepsilon_{\text{elo}}(\theta_{\text{app}}) z[h, \theta(\theta_{\text{app}})], \quad (\text{B2})$$

as a function of the altitude h and the apparent angle θ_{app} . Replacing $\theta = \theta(\theta_{\text{app}})$ and $z = z_{\text{ref}}/\varepsilon_{\text{elo}}(\theta_{\text{app}})$ in

$h(z, \theta)$, we get the altitude in terms of the refracted parameters, i.e.,

$$h = h_{\text{ref}}(z_{\text{ref}}, \theta_{\text{app}}) := h[z_{\text{ref}}/\varepsilon_{\text{elo}}(\theta_{\text{app}}), \theta(\theta_{\text{app}})]. \quad (\text{B3})$$

With these modifications in hand, we can formulate the refracted version of the atmospheric extinction in Eq. (10) of the main text. We need to integrate $\alpha(h) = \alpha_0 \exp(-h/\tilde{h})$ (with α_0 and \tilde{h} given in the main text) using the modified expression for the slant distance $z_{\text{ref}}(h, \theta_{\text{app}})$ and the expression of the altitude $h_{\text{ref}}(z_{\text{ref}}, \theta_{\text{app}})$. We get

$$\begin{aligned} \eta_{\text{atm}}^{\text{ref}}(h, \theta_{\text{app}}) &= \exp \left\{ - \int_0^{z_{\text{ref}}(h, \theta_{\text{app}})} dy \alpha[h_{\text{ref}}(y, \theta_{\text{app}})] \right\} \\ &= e^{-\alpha_0 g_{\text{ref}}(h, \theta_{\text{app}})}, \end{aligned} \quad (\text{B4})$$

where we have defined

$$g_{\text{ref}}(h, \theta_{\text{app}}) := \int_0^{z_{\text{ref}}(h, \theta_{\text{app}})} dy \exp \left[-\frac{h_{\text{ref}}(y, \theta_{\text{app}})}{\tilde{h}} \right]. \quad (\text{B5})$$

Correspondingly, we can modify the bound in Eq. (15) of the main text to account for refraction. We obtain

$$\begin{aligned} \mathcal{B}_{\text{ref}}(h, \theta_{\text{app}}) &= -\log_2 \left[1 - \eta_{\text{eff}} e^{-\alpha_0 g_{\text{ref}}(h, \theta_{\text{app}})} \right. \\ &\quad \times \left. \left(1 - e^{-\frac{2a_R^2}{w_d[z_{\text{ref}}(h, \theta_{\text{app}})]^2}} \right) \right]. \end{aligned} \quad (\text{B6})$$

For low transmissivity, which is certainly the case in the far field regime $z_R \gg 1$, we can approximate

$$\mathcal{B}_{\text{ref}}(h, \theta_{\text{app}}) \simeq \frac{2}{\ln 2} \frac{a_R^2 \eta_{\text{eff}} e^{-\alpha_0 g_{\text{ref}}(h, \theta_{\text{app}})}}{w_d[z_{\text{ref}}(h, \theta_{\text{app}})]^2}. \quad (\text{B7})$$

In Fig. 11, we investigate the effects of refraction on the channel loss. For typical parameters, we see that refraction is negligible within $\simeq 1$ radian from the zenith, while it becomes more and more relevant in the proximity of the horizon. For a sea-level ground station communicating with a satellite at $h = 780$ km and apparent zenith angle $\theta_{\text{app}}^{\max}$, we compute $\eta_{\text{atm}}^{\text{ref}} \simeq 7.1$ dB from Eq. (B4) instead of $\eta_{\text{atm}} \simeq 3.4$ dB from Eq. (10) of the main text (setting $\theta = \theta_{\text{app}}^{\max}$). This discrepancy leads to differences between \mathcal{B} and its refraction-based version \mathcal{B}_{ref} for large angles, i.e., close to the horizon.

Finally, it is worth mentioning that the formula in Eq. (B6) can also be applied to the case where the ground station is at some non-negligible altitude h_0 . In fact, it is sufficient to use Eqs. (A5) and (A6) in all the previous expressions that lead to Eq. (B6).

Appendix C: Atmospheric turbulence

1. Weak turbulence

Atmospheric turbulence leads different treatments depending on its strength. From a physical point of view,

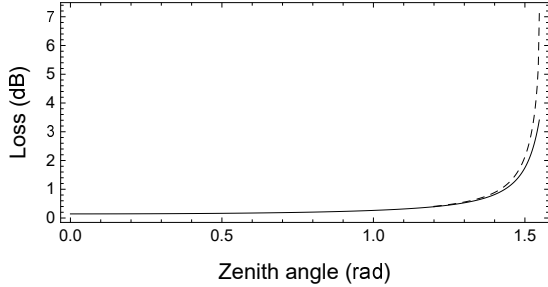


FIG. 11: Atmospheric loss (decibels) versus zenith angle (radians) in the link between a sea-level ground station and a satellite at $h = 780$ km, for $\lambda = 800$ nm. We plot the refraction-free model for atmospheric loss $-10 \log_{10} \eta_{\text{atm}}$ [given by Eq. (10) of the main text] with respect to the zenith angle θ (solid line), and the refraction-based model $-10 \log_{10} \eta_{\text{atm}}^{\text{ref}}$ of Eq. (B4) with respect to the apparent zenith angle θ_{app} (dashed line).

turbulence effects are due to eddies affecting the travelling beam. In a regime of weak turbulence, one can clearly distinguish the action of small and large turbulent eddies. Those smaller than the beam waist tend to broaden the beam (on a fast time scale), while those larger than the beam waist tend to deflect the beam, randomly but on a slower time scale [27]. As a result, the broadening of the beam can be decomposed into a sum of two contributions, the short-term spot size w_{st}^2 plus the random wandering of the beam centroid with variance σ_{TB}^2 , so that there is a long-term spot size [27, Eq. (32)]

$$w_{\text{lt}}^2 = w_{\text{st}}^2 + \sigma_{\text{TB}}^2. \quad (\text{C1})$$

The slower time scale is of the order of $10 - 100$ ms [28], which means that this dynamics can be resolved by a fast-enough detector.

If turbulence becomes stronger, the motion of the centroid becomes negligible and one has $w_{\text{lt}}^2 \simeq w_{\text{st}}^2$. At some point, strong beam deformation comes into place as a major effect, and the beam will eventually break up in multiple patches [27, 46].

The first step is therefore the correct characterization of the relevant regime of turbulence, which requires the introduction of parameters from the theory of optical propagation through turbulent media. The most important of these parameters is the refraction index structure constant C_n^2 [31, 47], since this is at the basis of the others and, in particular, the scintillation index [31], that characterizes the strength of turbulence, and the spherical-wave coherence length [27], that directly enters in the expressions of the spot sizes of Eq. (C1).

2. Refraction index structure constant

The structure constant C_n^2 measures the strength of the fluctuations in the refraction index, due to spatial varia-

tions of temperature and pressure. We need to consider an adequate model for the structure constant $C_n^2(h)$, so that this quantity can be suitably averaged over different altitudes for up- and down-link communication.

Assuming the Hufnagel-Valley (H-V) model of atmospheric turbulence [29, 30], the structure constant reads

$$C_n^2(h) = 5.94 \times 10^{-53} \left(\frac{v}{27} \right)^2 h^{10} e^{-h/1000} + 2.7 \times 10^{-16} e^{-h/1500} + A e^{-h/100}, \quad (\text{C2})$$

where $h > 0$ is expressed in meters, v is the windspeed (m/s) and A is the nominal value of $C_n^2(0)$ at the ground in units $\text{m}^{-2/3}$ (MKS units are implicitly assumed in all these formulas). These parameters depend on the atmospheric conditions and the time of the day.

Similarly to Ref. [28] one can assume the typical night-time value $A = 1.7 \times 10^{-14} \text{ m}^{-2/3}$ and low-wind $v = 21 \text{ m/s}$ [48]. This is also known as the H-V_{5/7} model [31, Sec. 12.2.1]. However, during the day, parameter A can be of the order of $2.75 \times 10^{-14} \text{ m}^{-2/3}$ [49] and, for high-wind conditions, v can be of the order of $v = 57 \text{ m/s}$ [22]. In our work, we adopt H-V_{5/7} as night-time model, and H-V with parameters $A = 2.75 \times 10^{-14} \text{ m}^{-2/3}$ and $v = 21 \text{ m/s}$ as day-time model. Finally, we may also consider H-V with parameters $A = 2.75 \times 10^{-14} \text{ m}^{-2/3}$ and $v = 57 \text{ m/s}$ as the worst-case day-time model.

It is important to remark that there are other models for $C_n^2(h)$. These include the VanZandt model [50], with a simplified version proposed by Dewan et al. [51], and the Walters and Kunkel model [52]. For instance, they have been used in Ref. [21, Appendix D]. These other approaches and the H-V model are in good agreement with thermosonde data in Ref. [53] (see also Ref. [21, Fig. 13]). Here we also consider a simplified version of this model, as originally proposed by Hufnagel and Stanley [29, Fig. 6]. This is given by [54, Eq. (3.1)]

$$C_n^2(h) \simeq c_1 h^{-1/3} \exp \left(-\frac{h}{c_2} \right), \quad (\text{C3})$$

$$c_1 = 4.2 \times 10^{-14}, \quad c_2 = 3200, \quad (\text{C4})$$

so that $C_n^2 \simeq 10^{-14} \text{ m}^{-2/3}$ a few meters high (see also Ref. [55, Ch. 3] and Ref. [56, Ch. 8]).

In Fig. 12, we show the H-V model of Eq. (C2) and the simplified Hufnagel-Stanley model in Eq. (C3) which are in good agreement. We can see that, at higher altitudes, C_n^2 starts to decrease exponentially. As a matter of fact, it can be considered to be negligible beyond $h_{\text{max}} \simeq 20$ km. This altitude corresponds to the upper edge of the tropopause, below which most of the mass of the atmosphere is contained. Taking h_{max} as effective thickness of the atmosphere can also be justified by the following argument. Let us treat the atmosphere as a single layer of thickness h and structure constant given by the average

$$\bar{C}_n^2(h) = h^{-1} \int_0^h d\xi C_n^2(\xi), \quad (\text{C5})$$

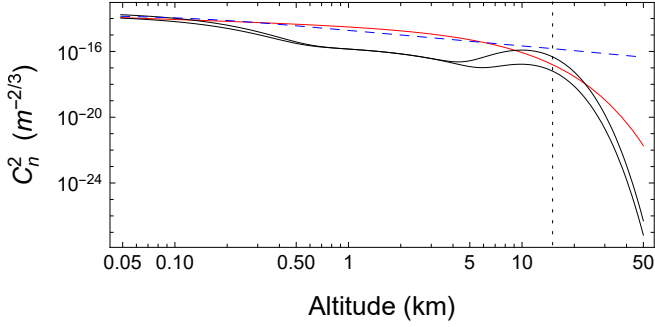


FIG. 12: Optical turbulence profile in the atmosphere, quantified by the refraction index structure constant C_n^2 as a function of the altitude h . More precisely, we plot the predictions of the Hufnagel-Valley model of Eq. (C2) (black curves) considering the typical night-time parameters (H-V_{5/7}, lower black curve) and the worst-case day-time parameters (i.e., the worst-case day-time model, upper black curve). We compare these predictions with the simplified model of Eq. (C3) (red curve), which is an approximate upper-bound at most altitudes. We can clearly see the exponential fall of $C_n^2(h)$ after $\simeq 15$ km (vertical dotted line), compared with the single-layer average value $\bar{C}_n^2(h)$ of Eq. (C5) (dashed blue line).

computed according to the standard H-V_{5/7} model. From Fig. 12, we can see how this quantity exponentially departs from the previous models after 15 km. At $\simeq 20$ km the difference is about two orders of magnitude.

For a satellite at altitude h and zenith angle $\theta \lesssim 1$ communicating with a sea-level ground station, the effective section of the atmosphere which is crossed by the beam is given by $z_{\text{atm}}(\theta) = z(h_{\text{max}}, \theta)$ using the slant functional in Eq. (A4). At one radiant, we have $z_{\text{atm}}(1) \simeq 37$ km, which is of the same order of magnitude of h_{max} . For larger angles, refraction comes into place and one needs to use the elongated slant distance in Eq. (B2). At the horizon, the section becomes large even neglecting the elongation by refraction. In fact, we have

$$z_{\text{atm}}(\pi/2) = \sqrt{h_{\text{max}}^2 + 2h_{\text{max}}R_{\text{E}}} \simeq 505 \text{ km.} \quad (\text{C6})$$

An important observation is that, for $\theta \lesssim 1$ and $h \leq h_{\text{max}}$, we may certainly use the approximations

$$z(h, \theta) \simeq h \sec \theta, \quad h(z, \theta) \simeq z \cos \theta, \quad (\text{C7})$$

since the relative error $[z(h, \theta) - h \sec \theta]/z(h, \theta)$ remains less than 0.4%. In the integral of Eq. (C5) the structure constant C_n^2 is non-negligible only for values $\xi \leq h_{\text{max}}$, so that we may write

$$\bar{C}_n^2(h) \simeq h^{-1} \int_0^{h_{\text{max}}} d\xi C_n^2(\xi) \simeq h^{-1} \int_0^{\infty} d\xi C_n^2(\xi). \quad (\text{C8})$$

This observation leads to a simplification when we write \bar{C}_n^2 and similar integrals in terms of the slant distance $z = z(h, \theta)$. In fact, for zenith angles $\theta \lesssim 1$, we may

write the approximation

$$\bar{C}_n^2(z, \theta) := z^{-1} \int_0^z dz' C_n^2[h(z', \theta)] \quad (\text{C9})$$

$$\simeq z^{-1} \sec \theta \int_0^h d\xi C_n^2(\xi). \quad (\text{C10})$$

3. Scintillation index and Rytov variance

An important issue in free-space communication with turbulence is the evaluation of the scintillation effects. In general, scintillation corresponds to irradiance fluctuations, causing variations of the field intensity across the aperture of the receiver, both temporally (twinkles) and spatially (speckles). As a result, for an input Gaussian beam, the intensity profile at the receiver will not be simply given by

$$I(z, r) = \frac{w_0^2}{w_d(z)^2} \exp[-2r^2/w_d(z)^2], \quad (\text{C11})$$

but there will be some instantaneous random profile $I(z, \mathbf{r})$, where $\mathbf{r} = (x, y)$ is the radial coordinate at the receiver and z the longitudinal coordinate.

Mathematically, one defines the scintillation index as the normalized variance of the field intensity [57]

$$\sigma_I^2(z, \mathbf{r}) := \frac{\langle I(z, \mathbf{r})^2 \rangle}{\langle I(z, \mathbf{r}) \rangle^2} - 1, \quad (\text{C12})$$

where the average is taken over the random fluctuations. This index is usually decomposed into a longitudinal (on-axis) and transverse (off-axis) parts [31, 57]

$$\sigma_I^2(z, \mathbf{r}) = \sigma_I^2(z, \mathbf{0}) + \sigma_{I,r}^2(z, \mathbf{r}). \quad (\text{C13})$$

The condition of weak fluctuation (weak turbulence) corresponds to $\sigma_I^2(z, \mathbf{r}) < 1$ throughout the beam profile. If this is the case, the mean intensity can be closely approximated by a Gaussian spatial profile [58–60].

According to previous studies [57, 61], the regime of weak turbulence holds for zenith angles smaller than 1 radiant (i.e., about 60°) assuming the standard H-V_{5/7} atmospheric model. For downlink, this is true for any beam waist w_0 . For uplink, the off-axis scintillation index $\sigma_{I,r}^2(z, \mathbf{r})$ increases with w_0 , but still remains reasonably small over the receiver's aperture if this is not too large (condition which is typically satisfied at the satellite). Under the assumption of weak fluctuations, one can use Rytov approximation for the beam field [62], together with the Kolmogorov power-law spectrum [63], and develop a simple formalism for the theory of turbulence.

In a weak-fluctuation theory, the longitudinal scintillation index $\sigma_L^2 := \sigma_I^2(z, \mathbf{0})$ can be easily written for both downlink and uplink. For a downlink path from a satellite at altitude h and zenith angle $\theta \lesssim 1$, this index equals

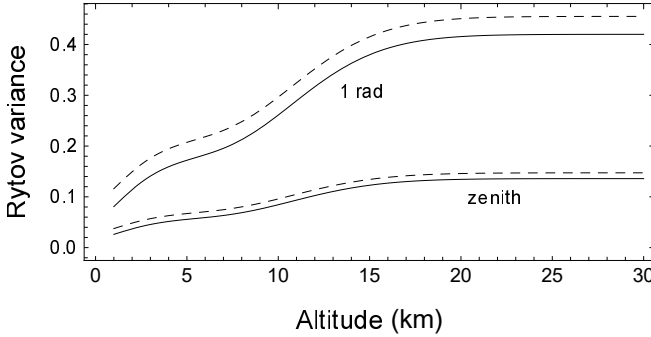


FIG. 13: Rytov variance versus altitude h (km) for $\theta = 0$ (zenith) and $\theta = 1$, considering $\lambda = 800$ nm. We plot the Rytov variance assuming the H-V model with night-time parameters (H-V_{5/7} model, solid lines) and the H-V model with typical day-time parameters (dashed lines). In all cases, the Rytov variance saturates at values that are < 1 .

the Rytov variance for a plane wave $\sigma_{R,\text{plane}}^2$, i.e. [31, 61]

$$\sigma_{L,\text{down}}^2 = \sigma_{\text{Rytov}}^2 := 2.25k^{7/6}h^{5/6}(\sec\theta)^{11/6}\mu(h), \quad (\text{C14})$$

$$\mu(h) := \int_0^h d\xi C_n^2(\xi) \left(\frac{\xi}{h}\right)^{5/6}. \quad (\text{C15})$$

Note that, if we impose C_n^2 to be constant in the integral of Eq (C15), then σ_{Rytov}^2 becomes $1.23C_n^2k^{7/6}z^{11/6}$, which is the expression for the Rytov variance that is valid for fixed-altitude z -long propagation.

For an uplink path, we may instead write [64]

$$\sigma_{L,\text{up}}^2 = \sigma_{L,\text{down}}^2 \frac{\tilde{\mu}(h)}{\mu(h)}, \quad (\text{C16})$$

$$\tilde{\mu}(h) := \int_0^h d\xi C_n^2(\xi) \left(\frac{\xi}{h}\right)^{5/6} \left(1 - \frac{\xi}{h}\right)^{5/6}. \quad (\text{C17})$$

As noted in Ref. [61], one can approximate $\tilde{\mu}(h) \simeq \mu(h)$, so that $\sigma_{L,\text{up}}^2 \simeq \sigma_{\text{Rytov}}^2$ also for uplink.

For these reasons the Rytov variance for a plane wave in Eq. (C14) can be used as a measure of the scintillation (in the weak fluctuation regime) and, most importantly, as a parameter to check if the condition of weak turbulence is indeed satisfied, corresponding to $\sigma_{\text{Rytov}}^2 < 1$. As we can see from Fig. 13, the value of the Rytov variance quickly saturates within the atmosphere and its values are below unity for zenith angles within 1 radian. It is easy to check that the Rytov variance exceeds 1 for larger zenith angles; for instance, at $h = 20$ km, we have that $\sigma_{\text{Rytov}}^2 > 1$ for $\theta \gtrsim 1.2$, i.e., beyond 69° . One can also check that, if we assume not typical but worst-case day-time parameters for the H-V model (i.e., high-wind conditions, see Appendix C 2), the Rytov variance tends to values that are below the unity at the zenith ($\simeq 0.6$), but quickly violate the unity for increasing zenith angle, e.g., $\simeq 2$ already at $\theta = 1$.

4. Coherence length

Once we have clarified the working regime of weak turbulence, we introduce the spherical-wave coherence length ρ_0 , which directly enters in the explicit expressions of the spot sizes of Eq. (C1). This is related to the well known Fried's parameter r_F [54, 65], that can be written as $r_F = 2.088\rho_0$ [32], and describes the transverse spatial separation at the receiver over which the field phase correlations decay by $1/e$. At the optical frequencies, typical values of ρ_0 or r_F are in cm. When this value is particularly large, e.g., of the order of meters, then the effects of turbulence are completely negligible from the point of view of the receiver. In this regard, we will see a stark difference between uplink and downlink.

For wavenumber k and propagation distance z , the spherical-wave coherence length is given by [27, Eq. (38)]

$$\rho_0 = [1.46k^2 I_0(z)]^{-3/5}, \quad (\text{C18})$$

$$I_0(z) := \int_0^z d\xi \left(1 - \frac{\xi}{z}\right)^{5/3} C_n^2(\xi), \quad (\text{C19})$$

where the explicit functional dependence of $C_n^2(\xi)$ needs to be specified and depends on the type of propagation. For free-space propagation at a fixed altitude, the value of C_n^2 is constant and we have the simple form

$$\rho_0^{\text{fix}} = (0.548k^2 C_n^2 z)^{-3/5}. \quad (\text{C20})$$

For uplink communications where the altitude h increases with the beam propagation, we assume the H-V_{5/7} model for $C_n^2(h)$ and we write ρ_0 in terms of the slant distance z and the zenith angle θ , by replacing $I_0(z)$ with the following integral

$$I_0^{\text{up}}(z, \theta) := \int_0^z d\xi \left(1 - \frac{\xi}{z}\right)^{5/3} C_n^2[h(\xi, \theta)], \quad (\text{C21})$$

where $h(z, \theta)$ is given in Eq. (A1). For downlink, the altitude decreases with the propagation. This is accounted by replacing $\xi \rightarrow z - \xi$ in the structure constant, so that we replace $I_0(z)$ with the following integral

$$I_0^{\text{down}}(z, \theta) := \int_0^z d\xi \left(1 - \frac{\xi}{z}\right)^{5/3} C_n^2[h(z - \xi, \theta)]. \quad (\text{C22})$$

In downlink, the term $(1 - \xi/z)^{5/3}$ goes to zero in the region where C_n^2 has the higher values (close to the ground). For this reason, the downlink coherence length ρ_0^{down} becomes large very quickly, for any object beyond the tropopause ($\simeq 20$ km). For instance, consider an object at the slant distance of $z = 100$ km sending down a beam with wavelength $\lambda = 800$ nm. We compute $\rho_0^{\text{down}} \simeq 1.8$ m at the zenith (compared to the uplink value $\rho_0^{\text{up}} \simeq 4.2$ cm) and $\rho_0^{\text{down}} \simeq 68$ cm at $\theta = 1$ (compared to $\simeq 2.9$ cm). At $\lambda = 1$ μm , we compute $\rho_0^{\text{down}} \simeq 2.4$ m at the zenith, and $\rho_0^{\text{down}} \simeq 0.9$ m at $\theta = 1$.

Note that these values increase both in distance z and wavelength. In particular, one has $\rho_0 \propto \lambda^{6/5}$.

It is clear that, within 1 radiant from the zenith (weak scintillation regime), the effect of the atmospheric turbulence is practically negligible in downlink paths. More precisely, this is true as long as the receiver's aperture a_R does not become too large. In fact, recall that the number of turbulence-induced short-term speckles from a point source is of the order of $N_s = 1 + (a_R/\rho_0)^2$ [31]. Assuming an aperture of $a_R = 40$ cm and an object at $z = 100$ km communicating at $\lambda = 800$ nm, we compute $N_s \simeq 1.05$ at the zenith and $\simeq 1.35$ at $\theta = 1$ radiant. These values are very close to the perfect coherent limit ($N_s = 1$). For these reasons, turbulence-induced beam spreading and wandering are negligible in downlink. This means that long- and short-term spot sizes are both equal to the diffraction-limited spot size, i.e., we can set $w_{lt} \simeq w_{st} \simeq w_d$.

For uplink the situation is completely different, and turbulence effects cannot be neglected even at the zenith position. Before proceeding further, it is important to note some simplifications which can be enforced for zenith angles $\theta \lesssim 1$ (that are useful for the spot sizes in uplink discussed in the next subsection). First of all, we may simplify the expression of the slant distance as in Eq. (C10) and write

$$\rho_0^{\text{up}} \simeq \left[1.46k^2 \sec \theta \int_0^h d\xi \left(1 - \frac{\xi}{h} \right)^{5/3} C_n^2(\xi) \right]^{-3/5}. \quad (\text{C23})$$

Then, we observe that, for $\theta \lesssim 1$, any satellite slant distance z is much larger than the thickness of the atmosphere ($20 - 37$ km). As a result, the term $(1 - \xi/z)^{5/3}$ in Eq. (C23) is $\simeq 1$ for all values of ξ falling in the atmosphere, where the quantity C_n^2 is non-negligible.

For this reason, we can approximate the spherical-wave coherence length ρ_0^{up} with a plane-wave coherence length [27, Eq. (51)], which is given by

$$\rho_p^{\text{up}} = [1.46k^2 I_p(z, \theta)]^{-3/5}, \quad (\text{C24})$$

$$I_p(z, \theta) = \int_0^z d\xi C_n^2[h(\xi, \theta)] \quad (\text{C25})$$

$$\simeq \sec \theta \int_0^h d\xi C_n^2(\xi). \quad (\text{C26})$$

This planar approximation is numerically investigated in Fig. 14, where we see how ρ_0^{up} rapidly approaches ρ_p^{up} already in the LEO region. These coherence lengths are computed using the exact integrals in Eqs. (C21) and (C25). The secant approximations in Eqs. (C23) and (C26) provide curves that are very close to those based on the exact integrals. As a matter of fact, they practically overlap with them at the zenith position. (Note that, while Fig. 14 is plotted for the night-time H-V model, an equivalent behaviour is found for the day-time H-V model, but with different asymptotic values).

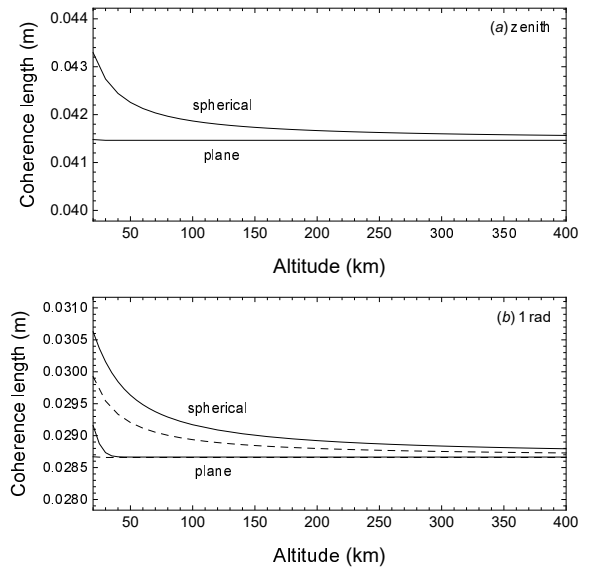


FIG. 14: Coherence length (m) versus altitude h (km) for uplink communication with a collimated Gaussian beam at $\lambda = 800$ nm. Turbulence is modelled by H-V_{5/7}. We compare the spherical-wave coherence length ρ_0^{up} (upper curve) and its plane-wave approximation ρ_p^{up} (lower curve). In panel (a), we consider the zenith position, while in panel (b) we consider $\theta = 1$. In both panels the solid curves are computed with the exact integrals in Eqs. (C21) and (C25). The dashed curves are associated with the secant approximations in Eqs. (C23) and (C26). The latter are not shown in panel (a) because they overlap with the solid curves. Note that ρ_0^{up} rapidly converges to ρ_p^{up} , and the asymptotic (lower bound) value in Eq. (C27) is approximately achieved already in the LEO region, i.e., for $h \geq h_{\text{LEO}} = 160$ km.

It is therefore clear that we can set $\rho_0^{\text{up}} \simeq \rho_p^{\text{up}}$ and use the integral in Eq. (C26). We can further simplify the formulas above by directly replacing the asymptotic value of the coherence lengths. In other words, we may extend the integral in Eq. (C26) to infinity, and write

$$\rho_0^{\text{up}} \simeq \rho_p^{\text{up}} \simeq [1.46k^2(\sec \theta)I_\infty]^{-3/5}, \quad (\text{C27})$$

$$I_\infty := \int_0^\infty d\xi C_n^2(\xi). \quad (\text{C28})$$

Assuming the H-V_{5/7} model of atmosphere ($A = 1.7 \times 10^{-14} \text{ m}^{-2/3}$ and $v = 21 \text{ m/s}$), particularly appropriate for night-time operation, we compute $I_\infty \simeq 2.2354 \times 10^{-12}$, so that

$$\rho_0^{\text{up}} \simeq \rho_p^{\text{up}} \simeq 8.59 \times 10^5 \lambda^{6/5} (\sec \theta)^{-3/5}, \quad (\text{C29})$$

which is an excellent approximation for any slant distance $z \geq h_{\text{LEO}} = 160$ km and zenith angle $\theta \lesssim 1$. For a day-time H-V model ($A = 2.75 \times 10^{-14} \text{ m}^{-2/3}$ and $v = 21 \text{ m/s}$), we compute the different value $I_\infty \simeq 3.2854 \times 10^{-12}$, so that the approximation in Eq. (C29) holds with a different prefactor.

5. Spot sizes for uplink

Consider a Gaussian beam with wavelength λ , spot size w_0 and curvature radius R_0 , which freely propagates in uplink for a distance z with a zenith angle $\theta \lesssim 1$, so that we are in the regime of weak turbulence. In particular, we may assume a collimated beam ($R_0 = +\infty$), even though this assumption is not necessary for the following theory. The associated spherical-wave coherence length ρ_0^{up} is based on the integral in Eq. (C21) which can be closely approximated by Eq. (C27).

We now impose Yura's condition [27, 33]

$$0.33 \left(\frac{\rho_0^{\text{up}}}{w_0} \right)^{\frac{1}{3}} \ll 1. \quad (\text{C30})$$

Using Eq. (C29), it is easy to show that Eq. (C30) is implied by $w_0^{1/3} \gg 31\lambda^{2/5}$, which is compatible with typical satellite communications. For instance, at $\lambda = 800$ nm, it means to considering spot sizes $w_0 \gg 1.4$ mm. Furthermore, the condition in Eq. (C30) could also be imposed more weakly as $\rho_0^{\text{up}}/w_0 < 1$, in which case the resulting expressions (discussed below) will be valid with a higher degree of approximation.

The satisfaction of Yura's condition in Eq. (C30) allows us to write the decomposition in Eq. (C1) with analytical expressions for the long- and short-term spot sizes. Specifically, we have the formulas [27, 33]

$$w_{\text{lt}}^2 \simeq w_{\text{d}}^2 + 2 \left(\frac{\lambda z}{\pi \rho_0^{\text{up}}} \right)^2, \quad (\text{C31})$$

$$w_{\text{st}}^2 \simeq w_{\text{d}}^2 + 2 \left(\frac{\lambda z}{\pi \rho_0^{\text{up}}} \right)^2 \Psi, \quad (\text{C32})$$

where w_{d} is the diffraction-limited field spot size and Ψ is given by [33]

$$\Psi = \left[1 - 0.33 \left(\frac{\rho_0^{\text{up}}}{w_0} \right)^{1/3} \right]^2 \simeq 1 - 0.66 \left(\frac{\rho_0^{\text{up}}}{w_0} \right)^{1/3}. \quad (\text{C33})$$

As a consequence, the variance associated to the centroid wandering is given by [33]

$$\sigma_{\text{TB}}^2 = w_{\text{lt}}^2 - w_{\text{st}}^2 \simeq \frac{0.1337 \lambda^2 z^2}{w_0^{1/3} (\rho_0^{\text{up}})^{5/3}}. \quad (\text{C34})$$

Note that the expressions in Eqs. (C31) and (C32) are derived from Ref. [33, Eqs. (16-18)] and Ref. [27, Eq. (37)], changing their notation from intensity spot size (w_{int}) to field spot size ($w = \sqrt{2}w_{\text{int}}$). See also Refs. [66-69] for related derivations.

The formulas above undergo a great simplification by explicitly accounting for the asymptotic expression of the coherence length ρ_0^{up} given in Eq. (C27). Thus, for uplink satellite communications with zenith angle $\theta \lesssim 1$, we may

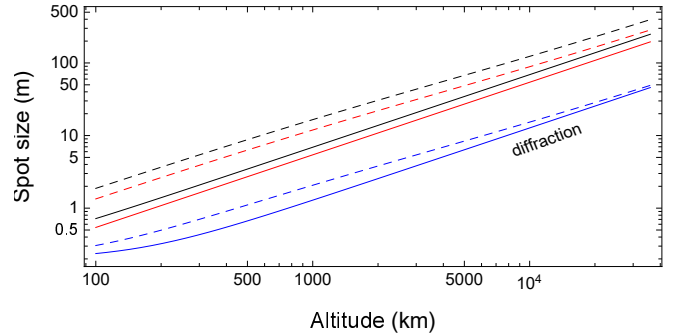


FIG. 15: Spot sizes (m) versus altitude h (km) for uplink communication by means of a collimated Gaussian beam with $\lambda = 800$ nm and $w_0 = 20$ cm. Turbulence is modelled by H-V_{5/7}. At the zenith position, we plot the short-term spot size w_{st} (black solid) and the standard deviation of the centroid wandering σ_{TB} (red solid), to be compared with the diffraction-limited spot size w_{d} (blue solid). Dashed lines refer to a zenith angle of $\theta = 1$.

write the following approximations

$$w_{\text{lt}}^2 \simeq w_{\text{d}}^2 + a \lambda^{-2/5} z^2 (\sec \theta)^{6/5}, \quad (\text{C35})$$

$$\Psi \simeq 1 - b w_0^{-1/3} (\lambda^2 \cos \theta)^{1/5}, \quad (\text{C36})$$

$$\sigma_{\text{TB}}^2 \simeq c w_0^{-1/3} z^2 \sec \theta, \quad (\text{C37})$$

where we set $a = 26.28 I_{\infty}^{6/5}$, $b = 0.2934 I_{\infty}^{-1/5}$ and $c = ab \simeq 7.71 I_{\infty}$, whose numerical values depend on the specific atmospheric profile (e.g., for the H-V_{5/7} model, they become $a \simeq 2.75 \times 10^{-13}$, $b \simeq 63$, and $c \simeq 1.72 \times 10^{-11}$). Then, for the short-term spot size, we may write the following simple expression

$$w_{\text{st}}^2 = w_{\text{lt}}^2 - \sigma_{\text{TB}}^2 \simeq w_{\text{d}}^2 + z^2 \Delta(\theta), \quad (\text{C38})$$

$$\Delta(\theta) := a \lambda^{-2/5} (\sec \theta)^{6/5} - c w_0^{-1/3} \sec \theta. \quad (\text{C39})$$

By using the geometric expression of the slant distance $z = z(h, \theta)$ from Eq. (A4) in Eqs. (C35), (C37) and (C38), we can study the behaviour of the spot sizes and that of the centroid wandering as a function of the altitude h and zenith angles $\theta \lesssim 1$. For a typical optical frequency, it is easy to see that their values practically coincide with those that can be computed from Eqs. (C31), (C32) and (C34), while providing much simpler analytical expressions. For uplink communication with a collimated beam with $w_0 = 20$ cm and $\lambda = 800$ nm, we perform a numerical study in Fig. 15. Here we note that the short-term spot size w_{st} becomes considerably larger than the diffraction-limited spot size w_{d} , and the standard deviation of the centroid wandering σ_{TB} increases from about $0.5 - 1$ m at the Kármán line to about $200 - 300$ m at the GEO altitude ($\simeq 36$ km), depending on the value of the zenith angle.

Appendix D: Background noise in satellite communications

Let us discuss the basic theoretical models which describe the background noise affecting satellite communications. With good approximation, both the Moon and the Earth can be considered to be Lambertian disks [70, 71]. This means that the scattering from their surfaces can be approximated to be uniform (radiance independent from the angle), which in turn implies that the intensity detected by the satellite's receiver strictly depends on its angular field of view Ω_{fov} .

First consider uplink. In day-time operation, the main source of noise comes from the sunlight directly reflected by the Earth towards the satellite. The total amount depends on the solar spectral irradiance H_{λ}^{Sun} at the relevant wavelength λ and the albedo of the Earth ($A_E \simeq 0.3$). During night-time operation, the noise is mainly due to the sunlight reflected by the Moon towards the Earth, and then from the Earth towards the satellite. Therefore, this noise also depends on the albedo of the Moon ($A_M \simeq 0.12$), the radius of the Moon ($R_M \simeq 1.737 \times 10^6$ m), and the average Earth-Moon distance ($d_{\text{EM}} \simeq 3.84 \times 10^8$ m).

Considering these parameters, the mean number of environmental thermal photons impinging on the satellite's receiver with aperture a_R and (solid) angular field of view Ω_{fov} , within the time window Δt and the spectral filter $\Delta\lambda$, is given by [72] $\bar{n}^{\text{up}} = \kappa H_{\lambda}^{\text{Sun}} \Gamma_R$. Here the parameter $\Gamma_R = \Delta\lambda \Delta t \Omega_{\text{fov}} a_R^2$ only depends on the specific features of the receiver, while the dimensionless factor κ is equal to $\kappa_{\text{day}} = A_E \simeq 0.3$ for day-time and to $\kappa_{\text{night}} = A_E A_M R_M^2 d_{\text{EM}}^{-2} \simeq 7.36 \times 10^{-7}$ for full-Moon night-time (roughly 10^{-6} of the day-time value).

At the optical regime, the typical values of \bar{n}^{up} are orders of magnitude higher than the photon numbers due to the black-body thermal radiation emitted by the Earth. Recall that the spectral radiance of a black body at tem-

perature T and wavelength λ is given by

$$N(\lambda, T) = 2c\lambda^{-4} \left[e^{hc/(\lambda k_B T)} - 1 \right]^{-1}, \quad (\text{D1})$$

in terms of number of photons per unit area, time, wavelength, and solid angle (photons $\text{m}^{-2} \text{s}^{-1} \text{nm}^{-1} \text{sr}^{-1}$). In the formula above, it is understood that c is the speed of light and k_B is the Boltzmann constant. Therefore, the total number of photons impinging on the receiver is given by $\bar{n}_{\text{body}}^{\text{up}} = N(\lambda, T) \Gamma_R$. Considering the optical wavelength $\lambda = 800$ nm and assuming the average surface temperature of the Earth ($T \simeq 288$ K), one has $N(\lambda, T) \simeq 3 \times 10^6$ photons $\text{m}^{-2} \text{s}^{-1} \text{nm}^{-1} \text{sr}^{-1}$. For a receiver with $\Gamma_R = 1.6 \times 10^{-19} \text{ m}^2 \text{s nm sr}$, we compute $\bar{n}_{\text{body}}^{\text{up}} \simeq 4.8 \times 10^{-13}$ mean photons, which is clearly negligible with respect to the values of \bar{n}^{up} given in the main text.

In downlink, the transmitter is the satellite and the receiver is a ground station with aperture a_R and angular field of view Ω_{fov} . In this case, the number of environmental photons reaching the receiver within the time window Δt and the spectral filter $\Delta\lambda$ is given by [22, 73] $\bar{n}^{\text{down}} = H_{\lambda}^{\text{sky}} \Gamma_R$, where $H_{\lambda}^{\text{sky}} := \pi \tilde{H}_{\lambda}^{\text{sky}} / (\hbar\omega)$ and $\tilde{H}_{\lambda}^{\text{sky}}$ is the background spectral irradiance of the sky in units $\text{W m}^{-2} \text{nm}^{-1} \text{sr}^{-1}$. In these units, its value ranges between 1.5×10^{-6} (full-Moon clear night) to 1.5×10^{-3} (clear day-time) and 1.5×10^{-1} (cloudy day-time) [73, Table 1], assuming that the field of view of the receiver does not include the Moon or the Sun [74, 75]. At $\lambda = 800$ nm, we have $\pi/(\hbar\omega) \simeq 1.27 \times 10^{19} \text{ W}^{-1} \text{s}^{-1} \text{sr}$, which means that H_{λ}^{sky} ranges between 1.9×10^{13} and 1.9×10^{18} photons $\text{m}^{-2} \text{s}^{-1} \text{nm}^{-1} \text{sr}^{-1}$. Using the same parameters for the receiver as above ($\Gamma_R = 1.6 \times 10^{-19} \text{ m}^2 \text{s nm sr}$), we find that \bar{n}^{down} ranges between $\simeq 3 \times 10^{-6}$ and $\simeq 0.3$ mean photons, which are the values for downlink reported in Table I of the main text.